Mineral-melt partitioning of redox-sensitive elements

Running head: Partitioning of redox-sensitive elements

Keywords: Oxygen fugacity, Partition coefficients, Multivalent elements, Magmatism

G. Mallmann[1*], A.D. Burnham[1], R.O.C. Fonseca[2]

[1] Research School of Earth Sciences, Australian National University, Canberra ACT 2601, Australia
*(corresponding author)
[2] Institute of Geology, Mineralogy and Geophysics Ruhr-University Bochum, Universitätsstr. 150, 44780 Bochum, Germany

Abstract

Elements with variable valence state (i.e. redox-sensitive) often show contrasting mineral/melt partition coefficients as a function of oxygen fugacity (fO_2) in magmatic systems. This is because trace-element incorporation into crystal lattices depends on the charge, size, and crystal-field stabilization energy of atoms, all of which differ greatly between oxidized and reduced species of the same element. This has two critical implications: (1) petrologic/ geochemical modelling of partitioning behavior of redox-sensitive trace-elements in magmatic systems requires some knowledge of their oxidation state, and (2) the oxidation state of magmatic systems may be inferred from partitioning relations of redox-sensitive trace elements preserved in mineral and melt phases of rapidly cooled magmas. The advantage of this oxybarometric approach is that mineral/melt partitioning relations are not sensitive to late stage degassing, charge-transfer on quenching, or surficial alteration. In this chapter we discuss the theoretical treatment of experimental mineral/melt partitioning data of redox-sensitive trace elements, and review aspects concerning the partitioning behavior of well-known redox-sensitive elements, including transition metals (Ti, V, Cr, Fe), rare earth elements (Ce, Eu), U, and siderophile elements (Mo, W, Re, and platinum group elements) under planetary magmatic fO_2 conditions.

1. Introduction

Although it is possible to determine valence-state ratios of redox-sensitive trace elements in natural and synthetic silicate glasses using techniques such X-ray absorption spectroscopy (e.g. Sutton and Newville, 2014), it may be challenging to relate these ratios to the oxygen fugacity (fO_2) of a silicate melt. This is because many elements exchange electrons with Fe, the most abundant redox-sensitive element in most magmas, upon quenching. For example, a mid-ocean ridge basaltic (MORB) melt at 1400 °C equilibrated at fO_2 equivalent to FMQ–1.7 (i.e. 1.7 log units below the fO_2 defined by the fayalite-magnetite-quartz buffer at the same temperature) has $Cr^{2+}/\Sigma Cr \sim 0.5$ (where $\Sigma Cr = Cr^{2+} + Cr^{3+}$), but upon quenching to a glass all the Cr^{2+} is converted to Cr^{3+} by reaction with Fe^{3+} (Berry et al., 2003):

$$Cr^{2+}_{melt} + Fe^{3+}_{melt} = Fe^{2+}_{glass} + Cr^{3+}_{glass} \quad (1)$$

Similar reactions with Fe have been documented for Eu and Ce (Burnham and Berry, 2014; Burnham et al., 2015), but because they require only the transfer of electrons, they are probably unavoidable. Consequently, valence-state ratios of trace elements in natural Fe-bearing glasses may not be representative of their high-temperature melt chemistry.

Provided that these elements are only present at low abundances relative to Fe, the exchange minimally affects the $Fe^{3+}/\Sigma Fe$ (where $\Sigma Fe = Fe^{2+} + Fe^{3+}$) of the magma. However, this ratio can still be affected by degassing of volatile species (e.g. Burgisser and Scaillet, 2007;

Mathez, 1984; Sato, 1978) as well as surficial oxidation (e.g. Rhodes and Vollinger, 2005). Sulfur degassing appears to be particularly important in the Earth because of the strong capacity of S to either reduce or oxidize Fe depending on the initial oxidation state of the magma (e.g. de Moor et al., 2013; Moussallam et al., 2016). For instance, the $Fe^{3+}/\Sigma Fe$ of reduced magmas, where S^{2-} (sulfide) is the dominant melt species, may be further reduced upon degassing of SO_2:

$$\underset{\text{melt}}{S^{2-}} + 3\,\underset{\text{melt}}{Fe_2^{3+}O_3} = \underset{\text{gas}}{S^{4+}O_2} + 6\,\underset{\text{melt}}{Fe^{2+}O} + \underset{\text{melt}}{O^{2-}} \quad (2)$$

whereas the $Fe^{3+}/\Sigma Fe$ of oxidized magmas, where S^{6+} (sulfate) is the dominant melt species, may be further oxidized upon degassing of SO_2:

$$\underset{\text{melt}}{S^{6+}O_4^{2-}} + 2\,\underset{\text{melt}}{Fe^{2+}O} = \underset{\text{gas}}{S^{4+}O_2} + \underset{\text{melt}}{Fe_2^{3+}O_3} + \underset{\text{melt}}{O^{2-}} \quad (3)$$

While potentially significant in their own right, such effects obscure the primary magmatic redox characteristics. In contrast, high-temperature distributions of trace elements between minerals and melts (i.e. partitioning relations) are readily preserved in rocks that have cooled at moderate or rapid rates, and hence allow the petrologist to 'see' melt chemistry that more accurately reflects the properties of the source of a magma. Furthermore, analysis of trace elements in minerals and glasses is readily achieved using benchtop equipment, unlike some spectroscopic techniques such as XANES that require access to the handful of suitably-equipped synchrotron beamlines worldwide. Hence, mineral/melt partitioning allows more convenient insights into the redox states of magmas.

To derive viable oxybarometers from mineral/melt partitioning, experimental data and a thermodynamic framework are required. Experimental equipment, such as gas-mixing tube furnaces, allows access to ~ 25 log units of fO_2 at 1400 °C; from 10 log units below the iron-wüstite buffer (IW–10) to six log units above the hematite-magnetite buffer (HM+6). For several redox-sensitive elements this is sufficient to encompass the entire transition from one valence state to another (where the redox reaction involves the exchange of 1 electron, such as Cr^{2+} to Cr^{3+}, the transition occurs over 16 log units, whereas for elements whose redox transition involves the exchange of 8 electrons, such as S^{2-} to S^{6+}, the transition occurs over 2 log units). This allows the partitioning behavior of the end-members to be determined. Nevertheless, in several cases it is not feasible to do this. For instance, where one valence state is highly volatile (e.g. Cr^{6+} or Mo^{6+}), or where an intermediate valence state always exists alongside a higher or lower valence state (e.g. V^{3+}, V^{4+} and U^{5+}), or when extreme redox conditions necessary to constrain the partitioning behavior of a valence state alone cannot be achieved in the laboratory. In such cases, it may be necessary to model the expected behavior of a valence state.

Lattice strain theory has become one of the fundamental concepts for understanding trace element partitioning into minerals (Blundy and Wood, 1994; Wood and Blundy, 2003). The essence of the theory is that substitution of a trace element i onto a cation site in a crystal lattice is energetically neutral if the substituent ion has the same ionic radius ($r_i = r_0$) and charge as the ion it replaces, resulting in a partition coefficient D_0. Where its ionic charge and/or radius differs, electrostatic work is done in repelling or attracting the adjacent anions (usually oxygen), and this work results in the trace element being less compatible than the one with optimal charge and radius, i.e. $D_i < D_0$. The dependence of log D_i on r_i is approximately parabolic; D_0 likewise has a quadratic dependence on atomic number, Z (Fig. 1). These two controlling variables are the reason that the various valence states of an element can have striking differences in their partitioning behavior. Consider the removal of an electron from Eu^{2+}:

$$Eu^{2+} = Eu^{3+} + e- \quad (4)$$

which not only increases the charge of the cation, but also (because of its higher effective nuclear charge) cause a contraction of the electronic orbitals, resulting in a decrease in ionic radius. This same principle applies to other major and trace elements capable of more than one valence state. As charge and ionic radius are principal controls on partitioning, it is almost inevitable that different valence states of an element will behave like different elements. Routine analytical techniques do not measure the speciation of redox-sensitive elements, which are usually reported as total concentrations without regard for the important differences between their valence states.

There are however challenges in the application of lattice strain theory to predict partition coefficients. These come mainly from crystal field effects and from the multitude of substitution mechanisms that are possible for a single cation in mineral sites.

Furthermore, there are important crystal-chemical implications for the fact that different valence states, such as Cr^{2+} and Cr^{3+}, behave like different elements. Crystals must have an overall neutral charge, hence when Cr^{2+} substitutes for Mg^{2+} in olivine, this criterion is observed, with the simple substitution $Mg^{2+} \leftrightarrow Cr^{2+}$ with the endmember Cr^{2+}-olivine forming according to the reaction:

$$\underset{\text{melt}}{2\,Cr^{2+}O} + \underset{\text{melt}}{SiO_2} = \underset{\text{olivine}}{Cr_2SiO_4} \quad (5a)$$

which, because forsterite (Mg_2SiO_4) saturation requires $2MgO + SiO_2$ and hence a fixed relationship between the activities of SiO_2 and MgO, can equivalently be written:

$$\underset{\text{melt}}{2\,Cr^{2+}O} + \underset{\text{olivine.}}{Mg_2SiO_4} = \underset{\text{melt}}{2\,MgO} + \underset{\text{olivine}}{Cr_2SiO_4} \quad (5b)$$

However, in order to substitute Cr^{3+} into the olivine structure, accommodation must be made for the difference in charge. One possibility involves the creation of vacancies [vac] on the octahedral site: $2\,Mg^{2+} \leftrightarrow 4/3\,Cr^{3+} + 2/3[vac]$. The reaction for formation of the corresponding endmember component is:

$$\underset{\text{melt}}{CrO_{1.5}} + 3/4\,\underset{\text{melt}}{SiO_2} = 3/4\,\underset{\text{olivine}}{Cr_{4/3}[vac]_{2/3}SiO_4} \quad (6)$$

Another possibility involves coupled substitution with Al and Si on the tetrahedral site: $Mg^{2+} + Si^{4+} \leftrightarrow Cr^{3+} + Al^{3+}$. The reaction for formation of the corresponding endmember component is:

$$\underset{\text{melt}}{CrO_{1.5}} + \underset{\text{melt}}{AlO_{1.5}} + 1/2\,\underset{\text{olivine}}{Mg_2SiO_4} = \underset{\text{olivine}}{MgCrAlO_4} + \underset{\text{melt}}{SiO_2} \quad (7)$$

Yet a third is tied to the incorporation of water:

$$\underset{\text{melt}}{CrO_{1.5}} + 0.5\,\underset{\text{melt}}{H_2O} + \underset{\text{melt}}{SiO_2} = \underset{\text{olivine}}{CrHSiO_4} \quad (8)$$

It can be seen from Equations 5-8, that these different substitutions each have their own dependence on the activity of SiO_2, and some additionally depend on the activities of Al_2O_3 and H_2O. Furthermore, other components in the melt (e.g. CaO) affect the activity coefficients of CrO and $CrO_{1.5}$, and accordingly the transition between Cr^{2+} and Cr^{3+} and their partition coefficients are also sensitive to melt composition (Berry et al., 2006). Consequently, the examples of partition coefficients quoted in this review should be taken as illustrative, rather than definitive.

In this chapter we summarize current knowledge on the effect of oxygen fugacity on the partitioning relations of redox-sensitive elements with relevant application to magmatic processes. We start by outlining some of the theoretical background behind the treatment of experimental partitioning data of redox-sensitive trace elements. This is followed by detailed sections on mineral/melt partitioning of transition metals (Ti, V, Cr, Fe), rare earth elements (Ce, Eu), uranium (U), and siderophile elements (Mo, W, Re, and platinum group elements).

2. Theoretical background

The bulk partition coefficient for a redox-variable element M (D_{M}) is given by the sum of the contributions from each valence state (a+, b+, c+), which is equivalent to the average of the partition coefficients for each valence state ($D_{\mathrm{M}^{a+}}$, $D_{\mathrm{M}^{b+}}$, $D_{\mathrm{M}^{c+}}$) weighted by their relative abundances:

$$D_{\mathrm{M}} = D_{\mathrm{M}^{a+}}\left(\frac{\mathrm{M}^{a+}}{\sum \mathrm{M}}\right) + D_{\mathrm{M}^{b+}}\left(\frac{\mathrm{M}^{b+}}{\sum \mathrm{M}}\right) + D_{\mathrm{M}^{c+}}\left(\frac{\mathrm{M}^{c+}}{\sum \mathrm{M}}\right) + \cdots \quad (9)$$

where $\sum \mathrm{M} = \mathrm{M}^{a+} + \mathrm{M}^{b+} + \mathrm{M}^{c+} + \cdots$. Any thermodynamic treatment of mineral/melt partitioning of redox-sensitive elements, however, requires that both the homogeneous redox equilibria between the components in the melt phase and the heterogeneous equilibria of the mineral-melt partitioning reaction are considered.

2.1. Homogeneous equilibria

The general reaction describing the oxidation of a redox-variable element M in a melt is:

$$\underset{\text{melt}}{\mathrm{M}^{x+}\mathrm{O}_{x/2}} + n/4\ \mathrm{O}_2 = \underset{\text{melt}}{\mathrm{M}^{(x+n)+}\mathrm{O}_{(x+n)/2}} \quad (10)$$

where x is the effective valence state of the metal cation M, and n is the number of electrons involved in the redox process. The equilibrium constant (K) for this homogeneous reaction is given by:

$$K_{10} = \frac{X_{\mathrm{M}^{(x+n)+}\mathrm{O}_{(x+n)/2}}\gamma_{\mathrm{M}^{(x+n)+}\mathrm{O}_{(x+n)/2}}}{X_{\mathrm{M}^{x+}\mathrm{O}_{x/2}}\gamma_{\mathrm{M}^{x+}\mathrm{O}_{x/2}}(\mathrm{fO}_2)^{n/4}} \quad (11)$$

where X is mole fraction and γ is the activity coefficient of each component relative to the standard states implicit in the definition of the Gibb's free energy of the reaction at the temperature of interest. Assuming that, for the low concentrations of trace elements, the activity coefficients are constant for a given composition (Henry's Law), the expression may be simplified to:

$$K'_{10} = \left(\frac{[\mathrm{M}^{(x+n)+}\mathrm{O}_{(x+n)/2}]}{[\mathrm{M}^{x+}\mathrm{O}_{x/2}]}\right)(\mathrm{fO}_2)^{-n/4} \quad (12)$$

where $K'_{10} = K_{10}/(\gamma_{M^{(x+n)+}O_{(x+n)/2}}/\gamma_{M^{x+}O_{x/2}})$ and the values in square brackets represent concentrations converted from mole fractions (note that the conversion factor from mole fractions to concentration cancels out between the numerator and denominator in the quotient). Taking the logarithm of this equation and re-arranging gives:

$$\log\left(\frac{[M^{(x+n)+}O_{(x+n)/2}]}{[M^{x+}O_{x/2}]}\right) = \frac{n}{4}\log fO_2 + \log K'_{10} \quad (13)$$

In the case where only two valence states are possible in the melt, by defining $\sum M = M^{x+} + M^{(x+n)+}$, one obtains:

$$\frac{M^{x+}}{\sum M} = \frac{1}{1 + 10^{(n/4 \log fO_2 + \log K'_{10})}} \quad (14a)$$

and

$$\frac{M^{(x+n)+}}{\sum M} = \frac{1}{1 + 10^{-(n/4 \log fO_2 + \log K'_{10})}} \quad (14b)$$

From this equation, it can be seen that $M^{x+}/\sum M$ takes a sigmoidal form, constrained to vary from 0 to 1, with log fO_2. The slope is defined by $n/4$ (i.e. the number of electrons in the redox reaction), and the position in log fO_2 space over which the transition from one valence state to the other occurs is determined by log K'_{10} (i.e. the simplified equilibrium constant for the homogeneous redox reaction). For elements such as U and V, which have three and four possible valence states in the melt, $\sum M \neq M^{x+} + M^{(x+n)+}$; instead, more complicated formulations are required. In the case of Cr, which can occur as Cr^{2+}, Cr^{3+} and Cr^{6+}, there is essentially no coexistence of Cr^{2+} and Cr^{6+}, and hence Equations 14a,b are valid approximations.

The above treatment groups all M^{x+} together. However, from a melt structural viewpoint, it has been argued that Fe^{3+} and Eu^{3+} occur both as dissociated cations and in complexes such as FeO_2^- and EuO_2^- (Fraser, 1975; Ottonello et al., 2001). Although it would be possible to write separate reactions for oxidation of Fe^{2+} to Fe^{3+} and FeO_2^-, the resulting equations would have an identical mathematical form to the simple model we present here. Our activity coefficients, and the use of a modified equilibrium constant log K'_{10}, accommodate the terms that would be necessary to account for the speciation of the participating ions. The use of a more refined structural model may, however, prove advantageous in describing the dependence of log K'_{10} on melt composition. This is addressed in greater detail in Moretti (this volume).

2.2. Heterogeneous equilibria

In the mineral (min) phase, the concentration of M will be given by the sum of all possible valence states, each with its own partitioning reaction:

$$M^{x+}_{mineral} = [M^{x+}O_{x/2}]_{melt} + \sum_{melt}[N^{x+}O_{x/2}] \quad (15)$$

where $N^{x+}O_{x/2}$ are the 'stoichiometric' control needed to form the phase component in which $M^{x+}O_{x/2}$ occurs (O'Neill and Eggins, 2002). The equilibrium constant for this heterogeneous reaction is given by:

$$K_{15} = \frac{X^{\min}_{M^{x+}} \gamma^{\min}_{M^{x+}O}}{X^{melt}_{M^{x+}O_{x/2}} \gamma^{melt}_{M^{x+}O_{x/2}} \prod a^{melt}_{N^{x+}O_{x/2}}} \quad (16)$$

where, $\prod a_{N^{x+}O_{x/2}}$ is the product of the activities of the components $N^{x+}O_{x/2}$ that make up the 'stoichiometric control' in the melt. The mineral/melt partition coefficient for each valence state of M is given by:

$$D_{M^{x+}} = \frac{\gamma^{\min}_{M^{x+}O}}{K_{15}\left(\gamma^{melt}_{M^{x+}O_{x/2}} \prod a^{melt}_{N^{x+}O_{x/2}} c\right)} \quad (17)$$

where c is a constant to convert mole fractions to concentrations by weight. From this equation, it becomes clear that the mineral/melt partitioning of M will depend on the activities of the major element oxides in the system, even if they mix ideally.

2.3. Mineral/melt partitioning as a function of fO_2

The mineral/melt partition coefficient of a redox-sensitive element M at constant pressure, temperature, and major element composition can be defined (alternatively to Equation 9) as the sum of the concentrations of all valence states in the mineral phase, divided by the sum of the concentration of all valence states in the melt phase:

$$D_M = \frac{\sum[M^{x+}_{min}]}{\sum[M^{x+}_{melt}]} \quad (18)$$

Assuming that M occurs in the valence states 1+, 2+, 3+…, this equation can be re-arranged to:

$$D_M = \frac{\frac{[M^{1+}_{min}]}{[M^{1+}_{melt}]} + \frac{[M^{2+}_{min}]}{[M^{1+}_{melt}]} + \frac{[M^{3+}_{min}]}{[M^{1+}_{melt}]} \ldots}{1 + \frac{[M^{2+}_{melt}]}{[M^{1+}_{melt}]} + \frac{[M^{3+}_{melt}]}{[M^{1+}_{melt}]} \ldots} \quad (19)$$

Homogeneous redox reactions can be written relating the different valence states to either the more reduced or oxidized end-members:

$$M^{1+}O_{0.5} + 1/2\, O_2 = M^{3+}O_{1.5} \quad (20a)$$
$$M^{1+}O_{0.5} + 1/4\, O_2 = M^{2+}O \quad (20b)$$
…

and the ratios of the concentrations of these related to K' and fO_2 in the following way:

$$[M^{3+}_{melt}]/[M^{1+}_{melt}] = (fO_2)^{0.5}\, K'_{20a} \quad (21a)$$

$$\left[\mathrm{M}^{2+}_{\mathrm{melt}}\right]/\left[\mathrm{M}^{1+}_{\mathrm{melt}}\right] = (\mathrm{fO_2})^{0.25}\, K'_{20\mathrm{b}} \quad (21\mathrm{b})$$

…

Substituting Equation 21 into Equation 19 and re-arranging gives:

$$D_M = \frac{\begin{array}{c} D^{1+} + [D^{2+}(\mathrm{fO_2})^{0.25} K'_{20\mathrm{b}}] \\ + [D^{3+}(\mathrm{fO_2})^{0.5} K'_{20\mathrm{a}}] + \cdots \end{array}}{\begin{array}{c} 1 + [(\mathrm{fO_2})^{0.25} K'_{20\mathrm{b}}] \\ + [(\mathrm{fO_2})^{0.5} K'_{20\mathrm{a}}] + \cdots \end{array}} \quad (22)$$

For convenience, this expression can also be written in the following form:

$$D_M = \frac{\begin{array}{c} D^{1+} + \left(D^{2+}\, 10^{0.25 \log \mathrm{fO_2} + \log K'_{20\mathrm{b}}}\right) \\ + \left(D^{3+}\, 10^{0.5 \log \mathrm{fO_2} + \log K'_{20\mathrm{a}}}\right) + \cdots \end{array}}{\begin{array}{c} 1 + \left(10^{0.25 \log \mathrm{fO_2} + \log K'_{20\mathrm{b}}}\right) \\ + \left(10^{0.5 \log \mathrm{fO_2} + \log K'_{20\mathrm{a}}}\right) + \cdots \end{array}} \quad (23)$$

which then allows for the log fO_2 term to be substituted more readily by oxygen fugacity terms relative to buffers in the customary way (e.g. ΔFMQ, ΔIW, etc.) as a form of minimizing the effect of temperature and pressure, if non-isobaric/isothermal data are considered.

3. Transition metals (Fe, Cr, Ti, V)

A large number of transition metals (those elements whose atoms have incompletely filled $3d$ orbitals) occur in more than one valence state under magmatic fO_2 conditions (Fig. 2). Amongst the redox-sensitive first-row transition metals, Fe is a major constituent of the solar system while others like Ti, V, and Cr occur in minor-to-trace concentrations (Palme and O'Neill, 2014). Mineral/melt partition relations of transition metals are harder to constrain in comparison with other trace elements as their behavior frequently does not obey Henry's Law. Furthermore, their electronic configuration results in strong crystal-field effects (Burns, 1993) and hence partitioning behavior is often anomalous in the context of lattice strain theory.

3.1. Iron (Fe)

As the only redox-sensitive cation that is a major element component in the solar system, iron has a fundamental role in magmatic redox processes. Arguably, fO_2 in the solid Earth is entirely controlled by the partitioning behavior of iron, which occurs as Fe^{3+} (ferric iron), Fe^{2+} (ferrous iron) as well as Fe^0 (metallic iron). The crystal-chemical controls on Fe partitioning are essential to understanding fO_2 throughout the Earth's mantle. For example, in the dominant upper mantle phase olivine (Mg_2SiO_4), iron occurs almost exclusively in the divalent form substituting for Mg in octahedral sites (i.e. $Fe^{3+}/\Sigma Fe \sim 0$; O'Neill et al. 1993). This means that, in a system closed to oxygen, a reduced basaltic melt that crystallizes olivine will become oxidized (i.e. its $Fe^{3+}/\Sigma Fe$ will increase). Conversely, an oxidized melt that crystallizes magnetite ($Fe^{2+}Fe^{3+}_2O_4$, with $Fe^{3+}/\Sigma Fe \sim 0.66$) will become reduced (i.e. its $Fe^{3+}/\Sigma Fe$ will decrease). Other ferromagnesian minerals in the upper mantle (e.g. pyroxenes, amphiboles, garnets) will also contribute to this mass balance.

Another fundamental example that illustrates the significance of crystal-chemical controls on the partitioning behavior of Fe comes from the most abundant mineral phase in the Earth's mantle, bridgmanite $(Fe,Mg)(Si,Al)O_3$. Bridgmanite can contain up to 20 atomic % Fe, a substantial proportion of which is trivalent ($Fe^{3+}/\Sigma Fe$ up to 0.6; McCammon, 1997; Frost et al., 2004). This preference of bridgmanite for ferric iron occurs because the coupled substitution of Fe^{3+} on to the VIII-fold coordinated Mg site, charge balanced by Al substitution on to the VI-fold coordinated Si site, is energetically favorable (Kesson et al., 1995). Therefore, Fe^{3+} occurs in experimentally grown Al-bearing bridgmanite even at very reducing conditions, with fO_2 maintained low via a disproportionation reaction that form metallic iron (e.g. Shim et al., 2017):

$$\underset{\text{bridgmanite}}{4\,{}^{\text{VIII}}(Fe^{2+}_{3/4}Al^{3+}_{1/4})^{\text{VI}}(Al^{3+}_{1/4}Si^{4+}_{3/4})O_3} = \underset{\text{bridgmanite}}{2\,{}^{\text{VIII}}(Fe^{3+})^{\text{VI}}(Al^{3+})O_3} + \underset{\text{stishovite}}{3SiO_2} + \underset{\text{metal}}{Fe^0} \qquad (24)$$

These types of disproportionation reactions are powerful in explaining the paradoxical evidence suggesting high Fe^{3+} contents in the very reduced lower mantle (McCammon, 2005).

In other abundant ferromagnesian minerals such as pyroxenes, the incorporation of Fe^{2+} and Fe^{3+} is also strongly dictated by stoichiometric controls. The experimental data of McCanta et al. (2004), for instance, highlight significant steric constraints on the substitution of Fe^{3+} for Fe^{2+} in pigeonite (low Ca clinopyroxene) compared to augite (high Ca clinopyroxene). The limited incorporation of Fe^{3+} into pigeonite is such that even under highly oxidizing conditions only a few percent of the total Fe will be trivalent. In contrast, alkali pyroxenes like aegirine ($NaFe^{3+}Si_2O_6$) have a strong affinity for Fe^{3+} but will not precipitate, even under oxidized conditions, unless there is sufficient Na available in the melt. As there is complete solid solution between augite and aegirine, Fe^{3+}/Fe^{2+} of a pyroxene has a complex dependence on melt composition when Fe is a major element, and lies beyond the scope of this discussion. A related issue arises with the partitioning of trace elements into magnetite, which is strongly fO_2-dependent. However, this is mostly due to the stoichiometric control by the Fe^{3+}/Fe^{2+} ratio of the melt rather than any variation in oxidation state of the trace elements themselves. For example, Ti becomes less compatible from FMQ to FMQ+4, well outside the range at which any Ti^{3+} is present, and this behavior is also exhibited by redox-invariant trace elements such as Zr and Hf (Sievwright et al., 2017). Hence, care should be taken when evaluating redox-related trends in Fe-rich systems to understand the factors contributing to variations in partition coefficients. The relationships described in this chapter are only applicable to trace components of melts and minerals.

Based on experiments with simplified synthetic compositions doped with small concentrations of Fe as a function of fO_2, Mallmann and O'Neill (2009) showed that $D_{Fe^{2+}} >> D_{Fe^{3+}}$ in olivine and orthopyroxene, but $D_{Fe^{2+}} < D_{Fe^{3+}}$ in clinopyroxene and spinel (Fig. 3a). Amphibole/melt data from King et al. (2000) indicates that the partitioning of both Fe^{3+} and Fe^{2+} are both close to unity, with $D_{Fe^{3+}}$ about a factor of two higher than $D_{Fe^{2+}}$ (though the range of fO_2 in this study, from FMQ-6 to FMQ+3, is not sufficient to constrain either Fe^{2+} or Fe^{3+}, so the differences in Ds between the two species are likely larger). The data of Martel et al. (1999) and Krawczynski et al. (2012), which examined fO_2 over an even more limited range alongside the effects of H_2O, T and P, show higher D_{Fe}/D_{Mg} at more oxidizing conditions, supporting a higher compatibility for Fe^{3+} in igneous amphiboles. It should be noted in passing that amphibole $Fe^{3+}/\Sigma Fe$ is readily altered by a redox reaction $Fe^{2+} + OH^- = Fe^{3+} + O^{2-} + ½\ H_2$, and hence may not preserve magmatic values (Popp et al., 1995).

In non-ferromagnesian minerals such as feldspars, iron behaves as a typical trace element. In plagioclase feldspar for instance (Fig. 3a), Fe^{3+} ($r^{VI} = 0.49$ Å)[1] is significantly more

[1] Ionic radii reported in this study were taken from Shannon (1976).

compatible than Fe^{2+} (Phinney, 1992; Wilke and Behrens, 1999) as it directly substitutes for Al^{3+} ($r^{IV} = 0.39$ Å) in tetrahedral sites, as opposed to Fe^{2+} which is significantly smaller ($r^{VIII} = 0.78$ Å) than the larger VIII-fold coordinated A-site ($r_0 \sim 1.2$ Å) (Longhi et al., 1976). In some oxidized peralkaline lavas, alkali feldspars with up to 2.8 wt.% Fe_2O_3 have been reported (Mann et al. 2006). Lundgaard and Tegner (2004) found a strong dependence of $D_{Fe^{2+}}$ and $D_{Fe^{3+}}$ on melt composition, particularly SiO_2, but not on plagioclase composition.

3.2. Chromium (Cr)

Chromium can exist as Cr^{2+}, Cr^{3+} and Cr^{6+} in magmas (e.g. Berry and O'Neill, 2004; Schreiber and Haskin, 1976), but direct detection of Cr^{2+} in quenched basaltic melts is hindered by an electron exchange with Fe on quenching (Reaction 1; Berry et al., 2003). Mineral-melt partitioning relations, however, have long indicated the presence of Cr^{2+} in silicate melts over typical magmatic conditions (e.g. Barnes, 1986; Hanson and Jones, 1998; Postovetov and Roeder, 2000). The divalent and trivalent species of Cr overwhelmingly dominate over typical magmatic fO_2s (Fig. 2), with hexavalent Cr only becoming stable at very oxidizing conditions (usually $>$ FMQ+4; Berry and O'Neill, 2004). Because such highly oxidizing conditions are uncommon in magmatic systems, and Cr^{6+} appears to be highly incompatible in high-temperature mineral phases (Mallmann and O'Neill, 2009), the presence of small amounts of Cr^{6+} in magmas should have no significant effect on the bulk partitioning of Cr (although it should be noted that the transition from Cr^{3+} to Cr^{6+} is expected to occur over a relatively narrow range of fO_2 given that the redox reaction involves three electrons). High-temperature experiments under the highly oxidizing conditions necessary to constrain the behavior of Cr^{6+} are limited (hexavalent Cr appears to be volatile at high temperature; Wijbrans et al., 2015), so the focus of our discussion will be on Cr^{2+} and Cr^{3+}.

Chromium is a major constituent of many rock-forming minerals (Burns and Burns, 1975), normally making end-member components where Cr^{3+} substitutes for Al^{3+} (and Fe^{3+}). Some of these substitutions are complete solid solutions, most notably between spinel ($MgAl_2^{3+}O_4$) and magnesiochromite ($MgCr_2^{3+}O_4$), and between grossular ($Ca_3Al_2^{3+}Si_3O_{12}$) and uvarovite ($Ca_3Cr_2^{3+}Si_3O_{12}$). In most cases, Cr^{3+} only occurs in octahedral coordination, as a result of its large crystal-field stabilization energy (CFSE; Burns, 1993). The ionic radius of Cr^{3+} is also significantly larger than Al^{3+} (and hence Si^{4+}), making it difficult for tetrahedral substitution. Incorporation of Cr^{2+} is unfavored due to its electronic configuration, which in octahedral coordination induces a destabilizing crystal-field energy and Jahn-teller distortions (Burns, 1975). Hence, Cr^{2+} can substitute for Mg^{2+} but only to a limited extent, and endmember Cr^{2+} silicates do not occur in nature (Li et al., 1995).

The importance of Cr to mantle phase equilibria (e.g. Liu and O'Neill, 2004), the link between chromite and precious metals (e.g. platinum group elements, PGE) in layered intrusions (e.g. Barnes, 1986), and its utility as an oxybarometer in magmatic systems (e.g. Postovetov and Roeder, 2000) has prompted numerous studies aimed at determining Cr solubility in silicate melts (e.g. Roeder and Reynolds, 1991) and its partitioning between associated phases. Here we focus on minerals where Cr substitutes as a trace component, as this allows us to constrain the effect of fO_2 on the partitioning behavior of both Cr^{2+} and Cr^{3+}.

Amongst minerals where Cr substitutes as trace element, olivine has the largest available experimental partitioning dataset as a function of fO_2. In olivine, Cr^{2+} ($r^{VI} = 0.80$ Å) is incorporated by direct replacement of Mg^{2+} ($r^{VI} = 0.72$ Å) in octahedral sites without significant lattice distortion (Reaction 5; Jollands et al., 2018). Substitution of Cr^{3+} ($r^{VI} = 0.615$ Å) into olivine octahedral sites, on the other hand, creates charge imbalance that can be accounted for either by octahedral vacancies (Reaction 6; Hanson and Jones, 1998; Jollands et al., 2018; Papike

et al., 2005), or by coupled substitution with Al^{3+} and Si^{4+} in tetrahedral sites (Reaction 7; Jollands et al., 2018).

Olivine/melt partitioning studies from Schreiber and Haskin (1976) and Hanson and Jones (1998) in the CaO-MgO-Al_2O_3-SiO_2 (CMAS) show a systematic dependence of $D_{Cr^{3+}}$ on melt composition (Fig. 4), though the dependence is not straightforward, suggesting that both substitution mechanisms described above likely operate. Hanson and Jones (1998), however, were able to parameterize $D_{Cr^{3+}}$ between olivine and melt using the universal melt descriptor NBO/T ($D_{Cr^{3+}} = -0.39\ \mathrm{NBO}/T + 1.29$). For Cr^{2+}, however, partitioning between olivine and melt appears to be independent of melt composition, but varies slightly with temperature (Hanson and Jones, 1998). More often than not, $D_{Cr^{2+}}$ is nearly equal to $D_{Cr^{3+}}$ between olivine and melt (including for basaltic compositions), so that effectively no change in bulk Cr partitioning is detected as a function of fO_2 (Mallmann and O'Neill, 2009; Hanson and Jones, 1998; Fig. 3b). Direct Cr valence measurements in olivine by XANES have confirmed these findings (Bell et al. 2014).

Mallmann and O'Neill (2009) found that Cr^{2+} is similarly partitioned amongst olivine, ortho- and clinopyroxene, but Cr^{3+} is significantly more compatible in pyroxenes, particularly clinopyroxene (Fig. 3b). This is not surprising given that Cr^{3+} ($r^{VI} = 0.615$ Å) has an ionic radius that is similar to the ideal strain-free octahedral M1 site of clinopyroxenes for trivalent cations ($r_0^{3+,M1} \sim 0.668$ Å; Hill et al., 2000). Cr^{2+} ($r^{VI} = 0.80$ Å), on the other hand, is significantly larger than the ideal M1 site of clinopyroxenes for divalent cations ($r_0^{2+,M1} \sim 0.69$ Å; Hill et al., 2000). Mallmann and O'Neill (2009) noted a significant difference between the partitioning of Cr^{3+} between clinopyroxene and melt obtained for their compositions V1 and V7 (which are identical except for the Cr-doping levels), suggesting that Cr^{3+} does not behave according to Henry's Law in the concentration range of these experiments (> 1.5 wt.%. Cr_2O_3), probably because of the strong coupling of Cr^{3+} with Al^{3+} in pyroxenes (Klemme and O'Neill, 2000). Chromium is noticeably more compatible in augite compared to pigeonite and enstatite, given the availability of cations (Al^{3+} and Na^{+}) for charge balancing the substitution of Cr^{3+} for Mg in octahedral sites (Karner et al., 2007; Mallmann and O'Neill, 2009). Interestingly, Cr^{2+} appears to be dominant species entering the structure of lower mantle phases such as ferropericlase and bridgmanite (Eeckhout et al., 2007). Neither Cr^{3+} nor Cr^{2+} appears to be easily incorporated into plagioclase (Aigner-Torres et al., 2007) as Cr^{3+} is too large for the tetrahedral site, and Cr^{2+} too small for the large distorted VIII-fold coordinated site.

Finally, we note that Cr is a well-known outlier in lattice-strain parabolas due to large crystal-field effects, so the prediction of Cr^{2+} and Cr^{3+} partitioning using lattice strain models should be done with great caution.

3.3. Titanium (Ti)

Titanium primarily occurs as Ti^{4+} over most of the range of fO_2s relevant to planetary scientists, but spectroscopic studies indicate that under very reducing conditions (i.e. below FMQ-4) a substantial fraction of Ti occurs as Ti^{3+} (Schreiber, 1977). The transition from Ti^{3+} to Ti^{4+} appears to be strongly dependent on melt composition (Borisov, 2012; Fig. 2). Hence, although the partitioning of Ti is a poor oxybarometer for terrestrial magmatism, it is markedly more relevant to understanding the geochemical evolution of the early solar nebula and reduced bodies such as the Moon (Fig. 2).

Hibonite ($CaAl_{12}O_{19}$) occurs in the calcium aluminum-rich inclusions (CAIs) of chondritic meteorites. It is one of the earliest phases to condense from the solar nebula, and can contain up to 8 wt% TiO_2 (Allen et al., 1978). The blue color of many hibonite grains has been shown to be due to the presence of Ti^{3+} (Burns and Burns, 1984; Sutton et al., 2017),

494 incorporated as a $CaTi_2^{3+}Al_{10}O_{19}$ component, but Ti^{4+} can also be accommodated in hibonite via
495 a coupled substitution with Mg, as a $CaMg_2Ti_2^{4+}Al_8O_{19}$component (Doyle et al., 2014). The
496 coupled nature of the substitution of Ti^{4+} means that the availability of Mg exerts a strong
497 control on $Ti^{3+}/\Sigma Ti$ (where $\Sigma Ti = Ti^{3+} + Ti^{4+}$) in hibonite; since it is often unclear which phases
498 are in equilibrium in CAIs, this oxybarometer may have limited utility (Berry et al., 2017).
499
500 Ti^{3+} is more compatible than Ti^{4+} in the majority of phases, including olivine, diopside,
501 orthopyroxene and anorthite (Mallmann and O'Neill, 2009; Peters et al., 1995; Fig. 3c). Ti K-
502 edge XANES measurements of both synthetic and natural lunar basalt samples have revealed
503 that Ti^{3+} is enriched in ilmenite, armalcolite and clinopyroxene at fO_2 of about FMQ-4.5 (Leitzke
504 et al., 2018; Simon and Sutton, 2018). However, as it is most compatible in clinopyroxene,
505 essentially all research has focused on this phase. Indeed, a Ti^{3+}-pyroxene (grossmanite,
506 $CaTi^{3+}AlSiO_6$) has been reported from the Allende meteorite, and $NaTi^{3+}Si_2O_6$ has been
507 synthesized experimentally (Ohashi et al., 1982; Ma and Rossman, 2009). Although quantitative
508 oxybarometry is hampered by multiple sources of uncertainty, including the equilibrium
509 mineral assemblage (as with hibonite), the mixing relations of Ti-bearing pyroxenes and the
510 temperature of formation, decreasing $Ti^{3+}/\Sigma Ti$ from core to rim of some CAIs suggests
511 increasingly oxidizing conditions in the solar nebula over a period of up to 300 kyr, perhaps by
512 as much as 6 – 7 log fO_2 units (Young et al., 2012). However, in some CAIs an oxidation trend,
513 followed by a more reduced rim, has been observed. This is attributed to incompatible Ti^{4+}
514 concentrating in the melt phase, which was isolated from the solar nebula by a thick melilite
515 mantle, followed by late-stage ingress of nebular gases to reduce the residual melt prior to
516 crystallization of the rims (Papike et al., 2016). Ti^{3+} has also been observed in lunar pyroxenes
517 (Burns et al., 1972), but is thought to be a minor component even on such a reduced planetary
518 body (Papike et al., 2005). Terrestrial magmas generally form at far more oxidizing conditions
519 and Ti is expected to occur exclusively as Ti^{4+} (Fig. 2). Pyroxenes in the native iron-bearing
520 lavas of Disko Island, Greenland, have been suggested to contain some Ti^{3+} (Pedersen, 1981),
521 but this is speculative and may not be compatible with the rather high Fe contents.
522
523
524 3.4. Vanadium (V)
525
526 Vanadium is the redox-sensitive trace element that occurs in the largest number of
527 valence states at typical magmatic fO_2s (Fig. 2), namely V^{2+}, V^{3+}, V^{4+} and V^{5+} (Borisov et al.,
528 1987; Schreiber et al., 1987; Sutton et al., 2005). Given the plethora of valence states with
529 theoretically contrasting geochemical behaviors, significant effort has been made to
530 characterize the effect of fO_2 and other variables such as pressure, temperature, mineral and
531 melt composition on the partitioning of V in silicate/oxide phases relevant to mantle melting
532 and magmatic differentiation (e.g. Arató and Audétat, 2017; Canil 1997; 1999; 2002; Canil and
533 Fedortchouk, 2000; 2001; Karner et al., 2008; Laubier et al., 2014; Mallmann and O'Neill, 2009;
534 2013; Papike et al., 2015; Righter et al. 2006a;b; 2011; Shearer et al., 2006; Sievwright et al.,
535 2017; Toplis and Corgne 2002; Wijbrans et al., 2015). The end goal of many of these studies is to
536 calibrate the sensitivity of V partitioning to fO_2 as an oxybarometer.
537
538 Under terrestrial magmatic fO_2 conditions (Fig. 2), V^{3+} and V^{4+} are the dominant valence
539 states, and spinel the major mineral group host. In pure magnetite ($Fe^{2+}Fe_2^{3+}O_4$), where the
540 stoichiometry fixes Fe^{3+}/Fe^{2+} at 2, incorporation of vanadium occurs via an fO_2-independent
541 electron-exchange reaction: $Fe^{3+} + V^{3+} = Fe^{2+} + V^{4+}$ (O'Neill and Navrotsky, 1984). However,
542 experimental studies of spinel group minerals have invariably shown strong dependence of
543 vanadium partitioning with fO_2 both in Fe-free and Fe-bearing systems (e.g. Arató and Audétat,
544 2017; Canil et al., 1999; Mallmann and O'Neill, 2009; Papike et al., 2015; Righter et al., 2006b;
545 Sievwright et al., 2017; Toplis and Corgne, 2002). Importantly, because Fe is an essential
546 component of magnetite, the partitioning of non-redox variable elements depends on fO_2

(Sievwright et al., 2017); this is not the case for Fe-poor spinels. For example, the ratio V^{3+}/V^{4+} of pure spinel ($MgAl_2O_4$) is controlled by the reaction:

$$1/2\ \underset{\text{spinel}}{MgV_2^{3+}O_4} + 3/2\ \underset{\text{melt}}{MgO} + 1/4\ \underset{\text{gas}}{O_2} = \underset{\text{spinel}}{Mg_2V^{4+}O_4} \quad (25)$$

It is therefore unsurprising that the bulk partitioning of V between spinel group minerals and silicate melt is a strong function of fO_2 as well as composition (mineral and melt). Experimental data shows that $D_{V^{3+}} >> D_{V^{4+}} > D_{V^{5+}}$ between spinel and silicate melt (Fig. 3d), and that the bulk partitioning of vanadium for Cr-spinels is higher than that for Al-spinels (Canil, 2002; Mallmann and O'Neill, 2009). The negative correlation between Al and V^{3+} in experimentally grown spinels provides strong evidence that the preferred mode of vanadium substitution into spinel is by direct replacement of Al in octahedral sites (Balan et al., 2006; Canil, 2002; Righter et al., 2006b). However, the details of the various possible substitution mechanisms are complex, given the structure of spinels and the multivalent nature of their cations (e.g. Papike et al., 2015). Melt composition also appears to play a significant role, as demonstrated by V partitioning experiments between magnetite and silicic melts (Arató and Audétat, 2017).

Owing to its high charge and small ionic radius, V^{5+} is highly incompatible in all rock-forming minerals. When sufficiently oxidized conditions are achieved, the partitioning of V^{5+} can be obtained, though this value is typically $<< 0.01$ (e.g. Mallmann and O'Neill, 2009). V^{4+} has partition coefficients that fall between V^{3+} and V^{5+} (Fig. 3d) and therefore is much harder to constrain. The ionic radius of V^{4+} is similar to that of Ti^{4+} in both octahedral and tetrahedral coordination ($r^{VI} = 0.58$ and 0.605 Å; $r^{IV} = 0.46$ and 0.42 Å; for V^{4+} and Ti^{4+} respectively), and both have similar electronic configurations and thus no significant difference in CFSE, so an approximation can be obtained using lattice strain theory. In connection with that, we note that $D_{V^{4+}}$ for pyroxene and olivine obtained by Mallmann and O'Neill (2009) are about an order of magnitude higher than what is inferred from lattice strain parabolas of other tetravalent cations. For some minerals, constraining the partitioning of V^{3+} may also be difficult when it shows compatibility between V^{2+} and V^{4+} (e.g. olivine or orthopyroxene). For clinopyroxene though, V^{3+} is clearly more compatible than both V^{2+} and V^{4+}, and its partitioning readily determined (Fig. 3d). Partition coefficients for V^{2+} can be obtained if sufficiently reduced experimental data is available, such as those reported by Mallmann and O'Neill (2009), but extrapolation from lattice strain parabolas should be avoided since V^{2+} has the same electronic configuration as Cr^{3+} and therefore large CFSE in octahedral coordination (Burns, 1993).

For mineral phases that only crystallize at high pressure from natural magmas, partitioning relations are harder to constrain as a function of fO_2 since this intensive parameter needs to be buffered externally using double-capsule techniques or internally using low-solubility solid metal-oxide. Righter et al. (2011) extended the fO_2 conditions obtained by Mallmann and O'Neill (2007, 2009) to constrain the $D_{V^{3+}}$ in garnet at ~ 10. The compatibility order of vanadium valences in garnet is $D_{V^{3+}} >> D_{V^{4+}} > D_{V^{5+}}$, with values comparable to clinopyroxene (Mallmann and O'Neill, 2009). XANES studies by Righter et al. (2011), however, suggest that small amounts of V^{2+} are incorporated into garnet, even under relatively oxidizing conditions.

Because of the complexities in developing a thermodynamic partitioning model that involves four different oxidation states, all of which likely varying differently with compositional parameters, Mallmann and O'Neill (2013) developed an empirical calibration of V partitioning between olivine and melt over a restricted range of fO_2s (from FMQ-4 to FMQ+4), where log D_V vary more or less linearly with log fO_2, accounting for the effects of olivine and melt composition. Similarly, Arató and Audétat (2017) developed an empirical calibration for magnetite. It would be useful to develop similar models for other common magmatic minerals, but this requires more extensive experimental databases since substitution of different V

valence states in minerals like pyroxene and garnet are more complex than in olivine and magnetite.

4. Rare earths (Ce and Eu)

The rare earth elements (REE), including Y, have favorable characteristics for examining redox processes. Apart from Ce and Eu, the REE exist exclusively in the trivalent state and their ionic radii vary smoothly from La to Lu (with Y somewhere between Ho and Er). This provides excellent coverage for fitting a lattice strain parabola to the REE^{3+}; anomalies relative to this parabola are readily quantifiable, and often visually striking. Zircon is notable because its REE patterns commonly feature both Ce and Eu anomalies (Fig. 5). They are typically quantified as Ce/Ce* and Eu/Eu*, where Ce* and Eu* are the values that would be predicted by interpolation or extrapolation. The simplest is the geometric mean of La and Pr (i.e., a linear interpolation on a logarithmic axis):

$$Ce^* = (La_N \times Pr_N)^{0.5} \quad (26)$$

where 'N' denotes normalization to CI chondrite, whole rock or matrix glass. La is often below the limit of detection for analyses of zircon, and so extrapolation from Pr-Nd-Sm may be used instead. Alternatively, polynomial fits to the REE pattern may be used (e.g. O'Neill, 2016; Burnham and Berry, 2017). There are systematic deviations between the methods, so values taken from different sources may need recalculation before being compared.

Cerium exists as both Ce^{3+} and Ce^{4+} in magmas. However, at typical magmatic fO_2 the proportion of Ce^{4+} is small (Fig. 2), with $Ce^{4+}/\Sigma Ce \sim 0.001$ (Burnham and Berry, 2012; 2014). At such low levels, it can be seen from Fig. 6a that where Ce^{4+} is less compatible than Ce^{3+} there is no perceptible effect on the bulk partitioning of Ce: even in the most extreme case, i.e. $D_{Ce^{4+}} = 0$, D_{Ce} would drop by 0.1 %, an amount that is far less than the achievable analytical accuracy. By a similar line of logic, it can be calculated that in order for a mineral in a terrestrial magma to develop a noticeable Ce anomaly, e.g. $Ce/Ce^* = 1.1$, $D_{Ce^{4+}}$ must be greater than $D_{Ce^{3+}}$ by a factor of 100. For minerals with a steep or strongly curved REE patterns, or larger analytical uncertainties, even a 10 % excess of Ce might not be a convincing anomaly.

Few minerals have a strong affinity for Ce^{4+}. The most notable, zircon, will be addressed in detail below. This is a favorable substitution on account of the identical 4+ charge of Zr, and a similarly large ionic radius ($r^{VIII} = 0.84$ and 0.97 Å for Zr and Ce^{4+} respectively). Positive Ce anomalies have been reported from other Zr minerals such as baddeleyite (Schärer et al., 2011), wadeite (Jaques, 2016), elpidite and armstrongite (Gerdes et al., 2017). Thomson et al. (2016) reported both positive and negative Ce anomalies for inclusions in diamonds, but the precise interpretation of these grains is complicated by their polymineralic nature and a lack of experimental partitioning data.

Zircon is the commonest of these, and has attracted the most experimental work (Burnham and Berry, 2012; Trail et al., 2011; 2012). The most recent calibration of the Ce-in-zircon oxybarometer uses lattice strain theory to infer $D_{Ce^{3+}}$ and $D_{Ce^{4+}}$, which allow $Ce^{4+}/\Sigma Ce$ in the melt to be calculated and the corresponding fO_2 deduced (Smythe and Brenan, 2016). This approach avoids the challenge of growing analyzable well-equilibrated zircon crystals, but there is presently a discrepancy between the two available models for Ce speciation in silicate melts (Burnham and Berry, 2014; Smythe and Brenan, 2015) and hence further work is required to develop a robust version of this oxybarometer.

For other minerals, these has been no systematic study of the effect of fO_2, but this can be predicted by a combination of lattice strain modelling (and for minerals with more than one

cation site, whose 4+ parabolas are underconstrained, by making the approximation $D_{Ce^{4+}} = D_{U^{4+}}$) and $Ce^{4+}/\Sigma Ce$ estimated from the optical basicity of the melt composition (Burnham and Berry, 2014). It can be seen that Ce^{4+} is less compatible than Ce^{3+} in Zr-free minerals and that, as explained above, D_{Ce} does not change appreciably in the fO_2 range of natural magmas.

Although the foregoing discussion considered mineral/melt partitioning, it is not always possible to consider mineral compositions in terms of mineral/melt partition coefficients. In particular, plutonic rocks do not retain any melt fraction, but even volcanic rocks often contain a significant cargo of crystals that are substantially older and may not be in equilibrium with their present host (e.g. Murphy et al., 1998). In the case of Ce, it is possible to use the bulk rock or even CI chondrite as a normalization factor, because magma compositions with Ce anomalies are uncommon. It is often stated that subduction zone magmas can have $Ce/Ce^* < 1$, indicating the incorporation of Ce-depleted sediments. As highlighted by O'Neill (2016), however, many reported examples of Ce anomalies in lavas are poorly constrained. Relatively small negative Ce anomalies, $Ce/Ce^* \sim 0.9$, are known in a variety of subduction settings (e.g. Hastie et al., 2009; Woodhead, 1989). As zircon Ce anomalies are typically one or two orders of magnitude larger, failure to account for a pre-existing Ce anomaly in the magma results in an underestimate of log fO_2 of < 0.2. The same is not true for Eu.

Europium can exist as Eu^{2+} and Eu^{3+} in magmas. The transition occurs most rapidly below the FMQ buffer, a range over which $Fe^{3+}/\Sigma Fe$ changes more slowly, and hence it is potentially a useful oxybarometer for reduced magmas (Fig. 2). The crystal chemistry of Eu^{2+} ($r^{VI} = 1.17$ Å) can be thought of as similar to Sr^{2+} ($r^{VI} = 1.18$ Å), and indeed there is even a Eu^{2+} feldspar (Kimata, 1988). In contrast, Eu^{3+} behaves as a typical middle REE. Accordingly, $D_{Eu^{2+}} > D_{Eu^{3+}}$ for plagioclase and alkali feldspars and åkermanitic melilite (Kuehner et al., 1989), but for most other minerals $D_{Eu^{3+}} > D_{Eu^{2+}}$ (Fig. 6b). Plagioclase feldspar and clinopyroxene are by far the most-studied in terms of Eu partitioning as a function of fO_2 and the following discussion will be restricted to these, although phases such as titanite, with $D_{Eu^{3+}}/D_{Eu^{2+}} \approx 2500$ may be important to consider for some igneous systems (Loader et al., 2017).

There are various models that allow plagioclase/melt $D_{Eu^{2+}}$ and $D_{Eu^{3+}}$ to be predicted using lattice strain theory (Aigner-Torres et al., 2007; Dohmen and Blundy, 2014). Corresponding models for clinopyroxene and other minerals have not been developed, and even in the case of plagioclase, Eu oxybarometry will be more precise where measured values of partition coefficients for proxy elements are used for $D_{Eu^{2+}}$ and $D_{Eu^{3+}}$. Rearranging Equation 9, we can approximate $Eu^{3+}/\Sigma Eu$ by:

$$Eu^{3+}/\Sigma Eu = (D_{Eu} - D_{Sr})/(D_{MREE} - D_{Sr}) \quad (27)$$

where D_{Eu} is the observed Eu partition coefficient and D_{MREE} is an estimate of $D_{Eu^{3+}}$, i.e. D_{Sm}, D_{Gd}, or preferably $(D_{Sm} \times D_{Gd})^{0.5}$. For values of $Eu^{3+}/\Sigma Eu$ in the range 0.1 to 0.9, the fO_2 can be calculated by rearranging the general equation from Burnham et al. (2015):

$$\log fO_2 = 40.4 - 25640/T - 56.8\Lambda - 4 \log (\Sigma Eu/Eu^{3+} - 1) \quad (28)$$

where T is temperature in Kelvin, and Λ is optical basicity, which can be calculated as:

$$\Lambda = \frac{\frac{SiO_2}{62.6} + \frac{TiO_2}{36.3} + \frac{Al_2O_3}{56.6} + \frac{FeO}{55.8} + \frac{MgO}{51.7} + \frac{CaO}{56.1} + \frac{Na_2O}{53.2} + \frac{K_2O}{67.3}}{\frac{SiO_2}{30.04} + \frac{TiO_2}{39.9} + \frac{Al_2O_3}{34} + \frac{FeO}{55.8} + \frac{MgO}{40.3} + \frac{CaO}{56.1} + \frac{Na_2O}{62} + \frac{K_2O}{94.2}} \quad (29)$$

with all oxide components in wt. %, and no distinction drawn between Fe^{2+} and Fe^{3+}. The effect of H_2O was not included in the optical basicity model of Duffy (1993) and hence is not considered here. At natural concentrations, MnO and P_2O_5 have negligible influence (e.g. 0.5 wt.% P_2O_5 would change log K' for Eu^{2+}-Eu^{3+} by ~0.02).

With values of $Eu^{3+}/\Sigma Eu$ outside the range 0.1 to 0.9, the reliability of this type of oxybarometer is compromised by the shallow slope of $M^{x+}/\Sigma M$ against fO_2. An error of ± 0.03 propagates to more than a log unit of fO_2. A key challenge in using Eu partitioning to determine fO_2 is the strong dependence of log K' on melt composition (Aigner-Torres et al., 2007; Burnham and Berry, 2015). The relationship given in Equation 28 was derived for alkali-free compositions, though experimental data for Na- and K-bearing compositions in the literature are generally consistent with this relationship. Moreover, although it lies outside the scope of this review, we note that in hydrothermal fluids the Eu^{2+}-Eu^{3+} equilibrium is 12 times more sensitive to pH than to log fO_2, and hence this variable must also be considered in low-temperature systems (Brugger et al., 2008).

5. Uranium (U)

Although it has been known for many years that U can exist as U^{4+}, U^{5+} and U^{6+} in silicate melts (e.g. Calas 1979; Schreiber 1983), this fact has often been rather under-appreciated in the geochemical literature. The radioactivity of U generates heat as well as a series of decay products culminating in Pb, and hence understanding the geochemistry of U is particularly important. Interpretation of U-series disequilibrium depends on accurate partition coefficients for U and Th (as well as other elements in the series). Because of potential differences in redox between mid-oceanic ridges and subduction zone settings, for example, it is essential to consider the role of fO_2 in controlling the partitioning of U relative to Th.

Partitioning of U as a function of fO_2 has only been studied for a handful of minerals (Fig. 7). Despite the importance of garnet in influencing U-series disequilibrium (Beattie, 1993), little is known about the how its partitioning of U might be affected by fO_2. For all minerals studied to date, it appears that $D_{U^{4+}} > D_{U^{5+}} > D_{U^{6+}}$. As with the intermediate oxidation states of V, the partitioning of U^{5+} is difficult to constrain without independent spectroscopic measurements of $U^{5+}/\Sigma U$ in the same melt composition. An additional complication arises because U^{6+} is volatile and is gradually lost from 1 atm experiments, leading to uncertainty on $D_{U^{6+}}$ because diffusion is unlikely to occur fast enough to keep crystals in equilibrium with the changing melt composition (Burnham and Berry, 2012).

Although there are insufficient data to develop a general expression for $U^{n+}/\Sigma U$ as a function of melt composition, temperature, pressure and fO_2, it is known that higher oxidation states are favored by lower temperatures and melts with higher optical basicities (Schreiber, 1983; Halse, 2014). Notably, U^{5+} appears to have a reduced stability field with increasing pressure (Halse, 2014): at higher pressure it appears that U^{4+} oxidizes directly to U^{6+}, leading to a sharper change in partition coefficients as a function of fO_2 (Mallmann et al., 2016).

U-Pb dating of zircon is widely regarded as one of the most reliable techniques for determining rock ages. For zircons younger than a few million years old, it becomes important to consider the contribution of ^{230}Th to the ingrowth of ^{206}Pb, because minerals for which U is less compatible than Th will develop a ^{206}Pb excess, and vice versa. Correcting for these consequences of U-series disequilibrium necessitates estimates of D_{Th}/D_U. U is more compatible than Th under reducing conditions, but much less compatible at high fO_2: the variation in terrestrial magmatic redox conditions equates to a ~ 100 kyr range of possible age corrections (McLean et al., 2011).

6. Siderophile elements (Mo, W, Re, Pt group elements)

Siderophile elements (i.e. those with strong tendency to alloy with Fe) are important tracers of planetary differentiation owing to their propensity of fractionating into planetary cores. Because of this, a great deal of effort has been made to investigate the behavior of these elements during core formation and to determine their valence state in silicate melts.

6.1. Molybdenum (Mo), tungsten (W) and rhenium (Re)

Mo, W and Re are known to occur in 4+ and 6+ valence states at fO_2s relevant to planetary magmatism (Cottrell et al., 2009; Ertel et al., 2001; Holzheid et al., 1994; O'Neill & Eggins, 2002; O'Neill et al., 2008; Righter et al., 2016; Wade et al., 2012; 2013). While the hexavalent state of Mo, W and Re is dominant over most planetary conditions (Fig. 2), the mineral/melt partitioning behavior of these elements is strongly controlled by their tetravalent state (Fig. 8).

A common feature of the partitioning behavior of Mo, W and Re is that their 4+ valence state is significantly more compatible in silicates and oxides (e.g. spinel) than their 6+ valence state, the latter of which being almost perfectly incompatible in crystalline phases. The relative compatibility in silicates and oxides tends to follow the order $D_{cpx} > D_{opx} > D_{olv} > D_{spl} \sim D_{plg}$, independently of valence state (Fonseca et al., 2014; Leitzke et al., 2016; 2017; Mallmann and O'Neill, 2007; Wijbrans et al., 2015). For all three elements, the difference between the mineral/melt partition coefficient of their reduced and oxidized species spans three to five orders of magnitude (Fig. 8). The difference in partition coefficients between the valence states is most pronounced for clinopyroxene, with $D_{6+} \sim 10^{-5}$ and $D_{4+} \sim$ 3-6. The compatibility of tetravalent Re, Mo and W in clinopyroxene results from the nearly ideal size of these cations (r^{VI} = 0.66 Å for W^{4+}, 0.65 Å for Mo^{4+} and 0.63 Å for Re^{4+}) relative to the octahedral M1 site ($r_0^{4+,M1} \sim$ 0.66 Å; Hill et al., 2000), which makes the substitution into clinopyroxene lattice energetically favorable. While the mineral/melt partitioning of Re^{4+} and Mo^{4+} were determined directly by experimental data at reducing conditions (Mallmann and O' Neill, 2007; Leitzke et al., 2017), data for W^{4+} was constrained by Fonseca et al. (2014) using a lattice strain fit to Ti, Hf, Zr and Re. This is because the extremely reducing conditions necessary to reduce all W^{6+} to W^{4+} cannot be achieved in the laboratory. The important conclusion of these studies is that the partitioning behavior of these elements in magmatic systems will be completely different depending on fO_2, with significant implications for comparing lunar vs. terrestrial, or oceanic vs. arc magmatism.

The effect of composition on the mineral/melt partitioning of Mo, W and Re in pyroxenes has been addressed in some studies. Hill et al. (2000) and Righter and Shearer (2003) found a negative correlation between $D_{Mo, W}$ and the Ca-Tschermak (CaTs) component in clinopyroxene. However, the opposite trend was found by Leitzke et al. (2017), who observed that the clinopyroxenes with the highest CaTs reported by Hill et al (2000) were formed from melt compositions with the highest CaO. Leitzke et al. (2017) speculated that, because the activity coefficients of MoO_3 and MoO_2 in silicate melts decrease with increasing CaO content (O'Neill and Eggins, 2002), the negative correlation found by Hill et al. (2000) could be due to the high CaO content of the silicate melt rather than pyroxene composition. Leitzke et al. (2016) investigated the effect of TiO_2 in the silicate melt, observing a positive correlation between the TiO_2 content of the melt on the partitioning of Mo^{4+} and W^{4+}, but little to no effect on the partitioning of Mo^{6+} and W^{6+} (perhaps because these cations are very incompatible). Conversely, partitioning coefficients for Hf and Zr decrease with TiO_2 content of the melt. (D_{Ti} remained constant, as expected for Henry's Law behavior). Leitzke et al. (2016) argued that the introduction of $CaTi^{4+}Al_2O_6$ into clinopyroxene with increasing melt TiO_2 raises elastic strain in

the M1 site of clinopyroxene. The increased elastic strain (which results in a tighter parabola) leads to an increase in the partitioning values of cations whose size are close to ideal for that site (e.g. W^{4+}), and a decrease in the partitioning values of those cations whose size are either smaller or larger than the ideal for that site (e.g. Zr^{4+} and Hf^{4+}).

6.2. Platinum Group Elements (Ru, Rh, Pd, Os, Ir, Pt)

There have been few studies investigating the redox-dependent partitioning behavior of the Platinum Group Elements (PGE) during magmatism, with most focusing on the role of base metal sulfides and, to a lesser extent, oxides. The scarcity of partitioning data arises from the low solubility of PGE in silicate melts (typically $<$ a few μg/g), especially under reducing conditions (O'Neill et al., 1995), and from the almost unavoidable presence of sub-micrometer metallic nuggets that plague the analyses of PGEs in synthetic silicate glasses and often lead to erroneous solubility values (Ertel et al., 2008). The solubility of a PGE in a silicate melt in equilibrium with metal can give an indication of its valence state(s), as it will dissolve according to Equation 10 (with $x = 0$ for the metal). However, despite significant effort in the last 20-30 years, PGE solubility results are still controversial. This leads to ambiguous interpretations regarding the PGE speciation as a function of fO_2. For example, solubility data for Ru are used to indicate that it either dissolves as Ru^{3+} (Borisov and Nachtweyh, 1998), or as both Ru^{3+} and Ru^{4+} (Laurenz et al., 2013) in silicate melts over planetary magmatic fO_2s. Similarly, Os appears to dissolve as Os^{3+} under most conditions, though the possibility of Os^{4+} being stable at more oxidizing conditions cannot be ruled out (Borisov and Walker, 2000; Fortenfant et al., 2006). Data for Ir are also ambiguous, indicating speciation as either Ir^{3+}, or combinations of Ir^{1+} - Ir^{3+} or Ir^{2+} - Ir^{3+} (Brenan et al., 2005; Borisov and Palme, 1995; Fonseca et al., 2011; O'Neill, 2015). Pt appears to occur exclusively as Pt^{2+}, except perhaps at very oxidizing conditions (FMQ $>$ 5) where Pt^{4+} may also be stable (Ertel et al., 1999). Of all PGEs, unambiguous evidence of redox-sensitivity over magmatic fO_2s only exists for palladium and rhodium, both of which occur as monovalent and divalent cations under typical magmatic fO_2s (e.g. Laurenz et al., 2010; Sommer, 2014; Fig. 2). Reports of other valence states for Pd and Rh in the literature arise from interpretation of micro(nano)nugget contaminated data (e.g. Borisov et al., 1994; Ertel et al., 1999).

Of the common magmatic minerals, spinel is the only mineral capable of accommodating significant amounts of PGEs, particularly Ru, Ir and Rh (e.g. Park et al., 2017). Wijbrans et al., (2015) reported a marked increase in D_{Rh} around FMQ in both Fe-free and Fe-rich spinels, indicating higher compatibility of Rh^{3+} relative to Rh^{2+}. Brenan et al. (2012) observed significant variations in the partitioning of several PGEs with fO_2 for Fe- and Cr-bearing spinels. However, as noted above, the partitioning of trace elements into magnetite is controlled by the Fe^{3+} and Fe^{2+} content of the melt, and it is often difficult to deconvolve this effect, and that of drastically changing site occupancies in the spinel from that of valence state changes in the trace element of interest. Nevertheless, the data in the Fe-free system are consistent with a change from Rh^{+} to Rh^{2+}, and also with olivine/melt partitioning data that shows decreasing D_{Rh} with increasing fO_2 (Brenan et al., 2003). Of the very few spinel/melt partitioning data available, Pd appears to be incompatible in spinel (Brenan et al., 2012).

7. Concluding remarks

In this chapter we have shown that the partitioning behavior of redox-sensitive trace elements will almost inevitably change with fO_2 in magmatic systems. This is because the incorporation of cations into crystal lattices (at constant pressure, temperature and composition) depends on their charge, size, and crystal-field stabilization energies, all of which

likely vary substantially between the oxidized and reduced species of the same element. This dependence on fO_2 means that petrologic/geochemical modelling involving elements such as Ti, Cr, V, Ce, Eu, U, Mo, Re, W, Pd, Rh (and probably others) must account for the oxidation state of the magma. As the only major-component redox-sensitive elements in many magmatic systems, the partitioning behavior of Fe is more likely to control rather than to reflect fO_2. Given the large range (10-15 order of magnitude; Fig. 2) of magmatic fO_2 in planetary systems, significant differences in the partitioning behavior of individual elements ought to be expected. For instance, several studies have shown that certain trace elements behave in completely different ways during lunar compared to terrestrial magmatism, or during magmatism in mid-ocean ridge compared to subduction zone settings.

Nevertheless, if the partitioning of redox-sensitive trace elements is determined experimentally as a function of fO_2 (and the effects of other parameters such as pressure, temperature and composition accounted for), then partitioning relations preserved in natural samples (e.g. glass and phenocryst in a volcanic rock) may provide useful ways of estimating the oxidation state of magmatic systems. This approach has the greatest advantage of being insensitive to late-stage degassing, charge-transfer (electron-exchange) reactions, or surficial alteration, all of which may potentially alter other magmatic redox proxies (e.g. $Fe^{3+}/\sum Fe$).

The preceding discussion demonstrates the importance of a good understanding of redox in modelling or interpreting trace element concentrations in melts and minerals. However, it should also be apparent that further work is required to bring our ability to model the partitioning of redox-variable elements. First, there are several elements for which very little information is available: most notably the PGEs, which have been investigated in surprisingly few minerals and whose redox transitions are poorly constrained. Copper was excluded from this review because of a paucity of data, but the data of Liu et al. (2014, 2015) indicate that its partitioning changes significantly from FMQ+1 to FMQ+5, a range that is highly relevant to arc environments where essentially all the world's economic Cu deposits are located. Likewise, experimental partitioning data by Mallmann and O'Neill (2009) indicate a potential change of phosphorus valence states from 5+ to 3+ under conditions below FMQ-4, but the results could also be explained by volatility loss from the melt after crystallization. And, under ultra-reducing conditions (~ FMQ-7), where Nb and Ta begin to show siderophile tendencies, there is evidence that they may take on lower valence states in silicate melts (Cartier et al., 2014).

Furthermore, the dependence of these redox transitions and partition coefficients on temperature and melt composition is complex, and only partially understood for the majority of the redox couples addressed here. As seen in Figure 4, melt composition affects the partitioning of different oxidation states of the same element in differing ways, an effect that is additional to the influence of stoichiometric controls on trace element partitioning. Similarly, melt compositional effects can shift the redox transition by up to 6 log units of fO_2 (Fig. 2). Because of these complications, extreme caution should be taken when attempting to study partitioning of redox-variable elements outside their calibrated ranges.

Many factors are important in selecting a mineral/melt partitioning oxybarometer. First, the anticipated redox state of the system will give an indication of which redox couples are relevant, but a large contrast between the compatibilities of the valence states of the element can sufficiently outweigh this consideration (for example, zircon will develop a Ce anomaly at conditions that are many orders of magnitude more reducing than the midpoint of the Ce^{3+}-Ce^{4+} equilibrium). The figures presented in this chapter may guide the geoscientist in determining whether the partition coefficient is likely to be sensitive to fO_2 for her or his samples. As emphasized above, the availability of appropriate experimental constraints is important, as are more general petrological considerations, for instance resistance to alteration processes such as

diffusive re-equilibration. In the ideal case, multiple elements and minerals would be combined to check for internal consistency.

Acknowledgments

We thank Aaron Bell and Roberto Moretti for their constructive comments. G.M. acknowledges funding of a Discovery Early Career Research Award from the Australian Research Council – ARC (grant DE160100169), A.B. acknowledges support from the ARC (grant FL130100066) and R.O.C.F. acknowledges funding of a Heisenberg Fellowship from the German Research Council – DFG (grants FO 698/5-1 and FO 698/11-1).

References

Aigner-Torres, M., Blundy, J., Ulmer, P., & Pettke, T. (2007). Laser ablation ICPMS study of trace element partitioning between plagioclase and basaltic melts: An experimental approach. *Contributions to Mineralogy and Petrology*, 153, 647-667.

Allen, J.M., Grossman, L., Davis, A.M., & Hutcheon, I.D. (1978). Mineralogy, textures and mode of formation of a hibonite-bearing Allende inclusion. 9th Lunar and Planetary Science Conference, 1209-1233.

Arató, R., & Audétat, A. (2017). Experimental calibration of a new oxybarometer for silicic magmas based on the vanadium partitioning between magnetite and silicate melt. *Geochimica et Cosmochimica Acta*, 209, 284-295.

Bachmann, O., Dungan, M.A., & Bussy, F. (2005). Insights into shallow magmatic processes in large silicic magma bodies: The trace element record in the Fish Canyon magma body, Colorado. *Contributions to Mineralogy and Petrology*, 149, 338-349.

Barnes, S.J. (1986). The distribution of chromium among orthopyroxene, spinel and silicate liquid at atmospheric pressure. *Geochimica et Cosmochimica Acta*, 50, 1889-1909.

Beattie, P. (1993). Uranium–thorium disequilibria and partitioning on melting of garnet peridotite. *Nature*, 363, 63-65.

Bell, A.S., Burger, P.V., Le, L., Shearer, C.K., Papike, J.J., Sutton, S.R., Newville, M., & Jones, J. (2014). XANES measurements of Cr valence in olivine and their application to planetary basalts. *American Mineralogist*, 99, 1404-1412.

Berry, A.J., & O'Neill, H.St.C. (2004). A XANES study of the oxidation state of chromium in silicate glasses. *American Mineralogist*, 89, 790-798.

Berry, A.J., O'Neill, H.St.C., Scott, D.R., Foran, G.J., & Shelley, J.M.G. (2006). The effect of composition on Cr^{2+}/Cr^{3+} in silicate melts. *American Mineralogist*, 91, 1901-1908.

Berry, A.J., Schofield, P.F., Kravtsova, A.N., Miller, L.A., Stephen, N.R., Walker, A.M., Soldatov, A.V., Ireland, T.R., Geraki, K. & Mosselmans, J.F.W. (2017). The limitations of hibonite as a single-mineral oxybarometer for early solar system processes. *Chemical Geology*, 466, 32-40.

Berry, A.J., Shelley, J.M.G., Foran, G.J., O'Neill, H.St.C., & Scott, D.R. (2003). A furnace design for XANES spectroscopy of silicate melts under controlled oxygen fugacities and temperatures to 1773 K. *Journal of Synchrotron Radiation*, 10, 332-336.

Blundy J., & Wood, B. (1994). Prediction of crystal-melt partition coefficients from elastic moduli. *Nature*, 372, 452-454.

Borisov, A.A. (2012). The Ti^{4+}/Ti^{3+} ratio of magmatic melts: application to the problem of the reduction of lunar basalts. *Petrology* 20, 391-398.

965 Borisov, A.A., Kadik, A.A., Zharkova, Ye., & Kalinichenko, N.V. (1987). Effects of oxygen fugacity
966 on the ratio between valency forms of vanadium in magmas. *Geokhimiya*, 7, 915-920.

967 Borisov, A., & Nachtweyh, K. (1998). Ru solubility in silicate melts: experimental results in
968 oxidizing region. 29th Lunar and Planetary Science Conference, 1320.

969 Borisov, A., & Palme, H. (1995). The solubility of iridium in silicate melts: new data from
970 experiments with $Ir_{10}Pt_{90}$ alloys. *Geochimica et Cosmochimica Acta*, 59, 481-485.

971 Borisov, A., & Walker, R. J. (2000). Os solubility in silicate melts: New efforts and results.
972 *American Mineralogist*, 85, 912-917.

973 Borisov, A., Palme, H., & Spettel, B. (1994). Solubility of palladium in silicate melts: Implications
974 for core formation in the Earth. *Geochimica et Cosmochimica Acta*, 58, 705-716.

975 Brenan, J. M., Finnigan, C. F., McDonough, W. F., & Homolova, V. (2012). Experimental
976 constraints on the partitioning of Ru, Rh, Ir, Pt and Pd between chromite and silicate melt:
977 The importance of ferric iron. *Chemical Geology*, 302, 16-32.

978 Brenan, J. M., McDonough, W. F., & Ash, R. (2005). An experimental study of the solubility and
979 partitioning of iridium, osmium and gold between olivine and silicate melt. *Earth and*
980 *Planetary Science Letters*, 237, 855-872.

981 Brenan, J. M., McDonough, W. F., & Dalpe, C. (2003). Experimental constraints on the
982 partitioning of rhenium and some platinum-group elements between olivine and silicate
983 melt. *Earth and Planetary Science Letters*, 212, 135-150.

984 Brugger, J., Etschmann, B., Pownceby, M., Liu, W., Grundler, P., & Brewe, D. (2008). Oxidation
985 state of europium in scheelite: Tracking fluid–rock interaction in gold deposits. *Chemical*
986 *Geology*, 257, 26-33.

987 Burgisser, A., & Scaillet, B. (2007). Redox evolution of a degassing magma rising to the surface.
988 *Nature*, 445, 194-197.

989 Burnham, A.D, & Berry, A.J. (2017). Formation of Hadean granites by melting of igneous crust.
990 *Nature Geoscience*, 10, 457-461.

991 Burnham, A.D., & Berry, A.J. (2012). An experimental study of trace element partitioning
992 between zircon and melt as a function of oxygen fugacity. *Geochimica et Cosmochimica Acta*,
993 95, 196-212.

994 Burnham, A.D., & Berry, A.J. (2014). The effect of oxygen fugacity, melt composition,
995 temperature and pressure on the oxidation state of cerium in silicate melts. *Chemical*
996 *Geology*, 366, 52-60.

997 Burnham, A.D., Berry, A.J., Halse, H.R., Schofield, P.F., Cibin, G., & Mosselmans, J.F.W. (2015). The
998 oxidation state of europium in silicate melts as a function of oxygen fugacity, composition
999 and temperature. *Chemical Geology*, 411, 248-259.

1000 Burns, R.G. (1975). On the occurrence and stability of divalent chromium in olivine included in
1001 diamonds. *Contributions to Mineralogy and Petrology*, 51, 213-221.

1002 Burns, R.G. (1993). *Mineralogical applications of crystal field theory*. 2nd Edition, Cambridge
1003 University Press, 551 p.

1004 Burns, R.G., & Burns, V.M. (1984). Crystal chemistry of meteoritic hibonites. *Journal of*
1005 *Geophysical Research*, 89, 313–321.

1006 Burns, R.G., Huggins, F.E. & Abu-Eid, R.M. (1972). Polarized absorption spectra of single crystals
1007 of lunar pyroxenes and olivines. *The Moon*, 4, 93-102.

1008 Burns, V.M., & Burns, R.G. (1975). Mineralogy of chromium. *Geochimica et Cosmochimica Acta*,
1009 39, 903-910.

1010 Calas, G. (1979). Etude expérimentale du comportement de l'uranium dans les magmas: États
1011 d'oxydation et coordinance. *Geochimica et Cosmochimica Acta*, 43, 1521-1531.

1012 Canil, D. (1997). Vanadium partitioning and the oxidation state of Archaean komatiite magmas.
1013 *Nature*, 389, 842-845.

1014 Canil, D. (1999). Vanadium partitioning between orthopyroxene, spinel and silicate melt and the
1015 redox states of mantle source regions for primary magmas. *Geochimica et Cosmochimica*
1016 *Acta*, 63, 557-572.

1017 Canil, D. (2002). Vanadium in peridotites, mantle redox and tectonic environments: Archean to
1018 present. *Earth and Planetary Science Letters*, 195, 75-90.

1019 Canil, D., & Fedortchouk, Y. (2000). Clinopyroxene-liquid partitioning for vanadium and the
1020 oxygen fugacity during the formation of cratonic and oceanic mantle lithosphere. *Journal of*
1021 *Geophysical Research*, 105, 26003-26016.

1022 Canil, D., & Fedortchouk, Y. (2001). Olivine-liquid partitioning of vanadium and other trace
1023 elements, with applications to modern and ancient picrites. *Canadian Mineralogist*, 39, 319-
1024 330.

1025 Canil., D. (1999). Vanadium partitioning between orthopyroxene, spinel and silicate melt and
1026 the redox states of mantle source regions for primary magmas. *Geochimica et Cosmochimica*
1027 *Acta*, 63, 557-572.

1028 Cartier, C., Hammouda, T., Boyet, M., Mathon, O., Testemale, D., & Moine, B.N. (2015). Evidence
1029 for Nb^{2+} and Ta^{3+} in silicate melts under highly reducing conditions: A XANES study.
1030 *American Mineralogist*, 100, 2152-2158.

1031 Cottrell, E., Walter, M.J., & Walker, D., (2009). Metal–silicate partitioning of tungsten at high
1032 pressure and temperature: Implications for equilibrium core formation in Earth. *Earth*
1033 *Planetary Science Letters*, 281, 275–287

1034 de Moor, J.M., Fischer, T.P., Sharp, Z.D., King, P.L., Wilke, M., Botcharnikov, R.E., Cottrell, E.,
1035 Zelenski, M., Marty, B., Klimm, K., Rivard, C., Ayalew, D., Ramirez, C., & Kelley, K.A. (2013).
1036 Sulfur degassing at Erta Ale (Ethiopia) and Masaya (Nicaragua) volcanoes: Implications for
1037 degassing processes and oxygen fugacities of basaltic systems. *Geochemistry, Geophysics,*
1038 *Geosystems*, 14, doi: 10.1002/ggge.20255

1039 Dohmen, R., & Blundy, J. (2014). A predictive thermodynamic model for element partitioning
1040 between plagioclase and melt as a function of pressure, temperature and composition.
1041 *American Journal of Science*, 314, 1319-1372.

1042 Doyle, P.M., Schofield, P.F., Berry, A.J., Walker, A.M., & Knight, K.S. (2014). Substitution of Ti^{3+}
1043 and Ti^{4+} in hibonite ($CaAl_{12}O_{19}$). *American Mineralogist*, 99, 1369-1382.

1044 Duffy, J.A. (1993). A review of optical basicity and its applications to oxidic systems. *Geochimica*
1045 *et Cosmochimica Acta*, 57, 3961-3970.

1046 Eeckhout, S.G, Bolfan-Casanov, N., McCammon C., Klemme, S., & Amiguet, E. (2007). XANES
1047 study of the oxidation state of Cr in lower mantle phases: Periclase and magnesium silicate
1048 perovskite. *American Mineralogist*, 92, 966-972.

1049 Ertel W., O'Neill H.St.C., Sylvester P.J., Dingwell D.B., & Spettel B. (2001). The solubility of
1050 rhenium in silicate melts: Implications for the geochemical properties of rhenium at high
1051 temperatures. *Geochimica et Cosmochimica Acta*, 65, 2161–2170

1052 Ertel, W., Dingwell, D. B., & Sylvester, P. J. (2008). Siderophile elements in silicate melts — A
1053 review of the mechanically assisted equilibration technique and the nanonugget issue.
1054 *Chemical Geology*, 248, 119-139.

1055 Ertel, W., O'Neill, H.St.C., Sylvester, P. J., & Dingwell, D.B. (1999). Solubilities of Pt and Rh in a
1056 haplobasaltic silicate melt at 1300 °C. *Geochimica et Cosmochimica Acta*, 63, 2439-2449.

1057 Fonseca, R.O.C., Mallmann, G., O'Neill, H.St.C., Campbell, I. H., & Laurenz, V. (2011). Solubility of
1058 Os and Ir in sulfide melt: Implications for Re/Os fractionation during mantle melting. *Earth*
1059 *and Planetary Science Letters*, 311, 339-350.

1060 Fonseca, R.O.C., Mallmann, G., Sprung, P., Sommer, J.E., Heuser, A., Speelmanns, I.M., & Blanchard,
1061 H. (2014). Redox controls on tungsten and uranium crystal/silicate melt partitioning and
1062 implications for the U/W and Th/W ratio of the lunar mantle. *Earth and Planetary Science*
1063 *Letters*, 404, 1-13.

1064 Fortenfant, S.S., Dingwell, D.B., Ertel-Ingrisch, W., Capmas, F., Birck, J.L., & Dalpe, C. (2006).
1065 Oxygen fugacity dependence of Os solubility in haplobasaltic melt. *Geochimica et*
1066 *Cosmochimica Acta*, 70, 742-756.

1067 Fraser, D.G. (1975). Activities of trace elements in silicate melts. *Geochimica et Cosmochimica*
1068 *Acta*, 39, 1525-1530.

1069 Frost, D.J., Liebske, C., Langenhorst, F., McCammon, C.A., Tronnes, R.G., & Rubie, D.C. (2004).
1070 Experimental evidence for the existence of iron-rich metal in the Earth's lower mantle.
1071 *Nature*, 428, 409-412.

1072 Gerdes, A., Kogarko, L.N., & Vladykin, N.V. (2017). New data on the age and nature of the Khan-
1073 Bogt alkaline granites, Mongolia. *Doklady Earth Sciences*, 477, 1320-1324.

1074 Grossman, L., Beckett, J.R., Fedkin, A.V., Simon, S.B., & Cieslan, F.J. (2008). Redox conditions in
1075 the solar nebula: Observational, experimental, and theoretical calculations. *Reviews in*
1076 *Mineralogy and Geochemistry*, 68, 93-140.

1077 Halse, H.R. (2014). *Using synchrotron radiation to determine the oxidation state of uranium in*
1078 *magmas*. PhD thesis, Imperial College London (http://hdl.handle.net/10044/1/19423).

1079 Hanson, B., & Jones, J.H. (1998). The systematics of Cr^{3+} and Cr^{2+} partitioning between olivine
1080 and liquid in the presence of spinel. *American Mineralogist*, 83, 669-684.

1081 Hastie, A.R., Kerr, A.C., Mitchell, S.F., & Millar, I.L. (2009). Geochemistry and tectonomagmatic
1082 significance of lower Cretaceous island arc lavas from the Devils Racecourse Formation,
1083 eastern Jamaica. *Geological Society London*, Special Publications, 328, 339-360.

1084 Hill, E., Wood, B.J., & Blundy, J.D. (2000). The effect of Ca-Tschermaks component on trace
1085 element partitioning between clinopyroxene and silicate melt. *Lithos*, 53, 203-215.

1086 Holzheid, A., Borisov, A., & Palme, H. (1994). The effect of oxygen fugacity and temperature on
1087 solubilities of nickel, cobalt and molybdenum in silicate melts. *Geochimimica et*
1088 *Cosmochimica Acta*, 58, 1975-1981

1089 Jaques, A.L. (2016). Major and trace element variations in oxide and titanate minerals in the
1090 West Kimberley lamproites, Western Australia. *Mineralogy and Petrology*, 110, 159-197.

1091 Jollands, M.C., O'Neill, H.St.C., Van Orman, J., Berry, A.J., Hermann, J., Newville, M., & Lanzirotti, A.
1092 (2018). Substitution and diffusion of Cr^{2+} and Cr^{3+} in synthetic forsterite and natural olivine
1093 at 1200-1500 °C and 1 bar. *Geochimica et Cosmochimica Acta*, 220, 407-428.

1094 Karner, J.M, Papike, J.J., Shearer, C.K., McKay, G., Le, L., and Burger, P. (2007). Valence state
1095 partitioning of Cr and V between pyroxene-melt: Estimates of oxygen fugacity for martian
1096 basalt QUE 94201. *American Mineralogist*, 92, 1238-1241.

1097 Karner, J.M., Papike, J.J., Sutton, S.R., Shearer, C.K., Burger, P., McKay, G., & Le, L. (2008). Valence
1098 state partitioning of V between pyroxene-melt: Effects of pyroxene and melt composition,
1099 and direct determination of V valence states by XANES. Application to Martian QUE 94201
1100 composition. *Meteoritics & Planetary Science*, 43, 1275-1285.

1101 Kesson, S.E., Fitzgeral, J.D., Shelley, J.M.G., & Withers, R.L. (1995). Phase relations, structure and
1102 crystal chemistry of some aluminous silicate perovskites. *Earth and Planetary Science*
1103 *Letters*, 134, 187-201.

1104 Kimata, M. (1988). The crystal structure of non-stoichiometric Eu-anorthite: An explanation of
1105 the Eu-positive anomaly. *Mineralogical Magazine*, 52, 257-265.

1106 King, P.L., Hervig, R.L., Holloway, J.R., Delaney, J.S., & Dyar, M.D. (2000). Partitioning of
1107 Fe^{3+}/Fe_{total} between amphibole and basanitic melt as a function of oxygen fugacity. *Earth and*
1108 *Planetary Science Letters*, 178, 97-112.

1109 Klemme, S., & O'Neill, H.St.C. (2000). The effect of Cr on the solubility of Al in orthopyroxene:
1110 Experiments and thermodynamic modelling. *Contributions to Mineralogy and Petrology*,
1111 140, 84-98.

1112 Krawczynski, M.J., Grove, T.L. & Behrens, H. (2012). Amphibole stability in primitive arc
1113 magmas: Effects of temperature, H_2O content, and oxygen fugacity. *Contributions to*
1114 *Mineralogy and Petrology*, 164, 317-339.

1115 Kuehner, S.M., Laughlin, J.R., Grossman, L., Johnson, M.L. & Burnett, D.S. (1989). Determination
1116 of trace element mineral/liquid partition coefficients in melilite and diopside by ion and
1117 electron microprobe techniques. *Geochimica et Cosmochimica Acta*, 53, 3115-3130.

1118 Laubier, M., Grove, T.L., & Langmuir, C.H. (2014). Trace element mineral/melt partitioning for
1119 basaltic and basaltic andesitic melts: An experimental and laser ablation ICP-MS study with
1120 application to the oxidation state of mantle source regions. *Earth and Planetary Science*
1121 *Letters*, 392, 265-278.

1122 Laurenz, V., Fonseca, R.O.C., Ballhaus, C., & Sylvester, P. J. (2010), Solubility of palladium in
1123 picritic melts: 1. The effect of iron. *Geochimica et Cosmochimica Acta*, 74, 2989-2998.

1124 Laurenz, V., Fonseca, R.O.C., Ballhaus, C., Jochum, K. P., Heuser, A., & Sylvester, P. J. (2013). The
1125 solubility of palladium and ruthenium in picritic melts: 2. The effect of sulfur. *Geochimica et*
1126 *Cosmochimica Acta*, 108, 172-183.

1127 Law, K.M., Blundy, J.D., Wood, B.J., & Ragnarsdottir, K.V. (2000). Trace element partitioning
1128 between wollastonite and silicate-carbonate melt. *Mineralogical Magazine*, 64, 651-661.

1129 Leitzke, F.P., Fonseca, R.O.C., Michely, L.T., Sprung, P., Münker, C., Heuser, A., & Blanchard, H.
1130 (2016), The effect of titanium on the partitioning behavior of high-field strength elements
1131 between silicates, oxides and lunar basaltic melts with applications to the origin of mare
1132 basalts. *Chemical Geology*, 440, 219–238

1133 Leitzke, F.P., Fonseca, R.O.C., Sprung, P., Mallmann, G., Lagos, M., Michely, L.T. & Münker, C.
1134 (2017). Redox dependent behaviour of molybdenum during magmatic processes in the
1135 terrestrial and lunar mantle: Implications for the Mo/W of the bulk silicate Moon. *Earth and*
1136 *Planetary Science Letters*, 474, 503-515.

1137 Leitzke, F.P., Fonseca, R.O.C., Göttlicher, J., Steininger, R., Jahn, S., Prescher, C., & Lagos, M.
1138 (2018). Ti K-edge XANES study on the coordination number and oxidation state of titanium
1139 in pyroxene, olivine, armalcolite, ilmenite, and silicate glass during mare basalt petrogenesis.
1140 *Contributions to Mineralogy and Petrology*, 173, 103.

1141 Li, J.P., O'Neill, H.St.C. & Seifert, F. (1995). Subsolidus phase relations in the system MgO-SiO_2-Cr-
1142 O in equilibrium with metallic Cr, and their significance for the petrochemistry of chromium.
1143 *Journal of Petrology*, 36, 107-132.

1144 Liu, X., & O'Neill, H.St.C. (2004). The effect of Cr_2O_3 on the partial melting of spinel-lherzolite in
1145 the system CaO-MgO-Al_2O_3-SiO_2-Cr_2O_3 at 1.1 GPa. *Journal of Petrology*, 45, 2261-2286.

Liu, X., Xiong, X., Audétat, A., Li, Y., Song, M., Li, L., Sun, W., & Ding, X. (2014). Partitioning of copper between olivine, orthopyroxene, clinopyroxene, spinel, garnet and silicate melts at upper mantle conditions. *Geochimica et Cosmochimica Acta*, 125, 1-22.

Liu, X., Xiong, X., Audétat, A., & Li, Y. (2015). Partitioning of Cu between mafic minerals, Fe–Ti oxides and intermediate to felsic melts. *Geochimica et Cosmochimica Acta*, 151, 86-102.

Longhi, J., Walker, D., & Hays, J.F. (1976). Fe and Mg in plagioclase. 7th Lunar and Planetary Science Conference, 1281-1300.

Lundgaard, K.L., & Tegner, C. (2004). Partitioning of ferric and ferrous iron between plagioclase and silicate melt. *Contributions to Mineralogy and Petrology*, 147, 470-483.

Ma, C., & Rossman, G.R. (2009). Grossmanite, $CaTi^{3+}AlSiO_6$, a new pyroxene from the Allende meteorite. *American Mineralogist*, 94, 1491-1494.

Mallmann, G., & O'Neill, H.St.C. (2007). The effect of oxygen fugacity on the partitioning of Re between crystals and silicate melt during mantle melting. *Geochimica et Cosmochimica Acta*, 71, 2837-2857.

Mallmann, G., & O'Neill, H.St.C. (2009). The crystal/melt partitioning of V during mantle melting as a function of oxygen fugacity compared with some other elements (Al, P, Ca, Sc, Ti, Cr, Fe, Ga, Y, Zr and Nb). *Journal of Petrology*, 50, 1765-1794.

Mallmann, G., & O'Neill, H.St.C. (2013). Calibration of an empirical thermometer and oxybarometers based on the partitioning of Sc, Y and V between olivine and silicate melt. *Journal of Petrology*, 54, 933-949.

Mallmann, G., Wykes, J., Berry, A.J., O'Neill, H.St.C., Cline II, C.J., Turner, S., & Rushmer, T.A. (2016). In situ XANES of U and Th in silicate liquids at high pressure and temperature. American Geophysical Union, Fall Meeting 2015, abstract MR13A-2418.

Mann, U., Marks, M., & Markl, G. (2006). Influence of oxygen fugacities on mineral compositions in peralkaline melts: The Katzenbuckel volcano, Southwest Germany. *Lithos*, 91, 262-285.

Martel, C., Pichavant, M., Holtz, F., Scaillet, B., Bourdier, J.L., & Traineau, H. (1999). Effects of fO_2 and H_2O on andesite phase relations between 2 and 4 kbar. *Journal of Geophysical Research: Solid Earth*, 104, 29453-29470.

Mathez, E.A. (1984). Influence of degassing on oxidation states of basaltic magmas. *Nature*, 310, 371-375.

McCammon, C. (1997). Perovskite as a possible sink for ferric iron in the lower mantle. *Nature*, 387, 694-696.

McCammon, C. (2005). The paradox of mantle redox. *Science*, 308, 807-808.

McCanta, M.C., Dyar, M.D., Rutherford, M.J., & Delaney, J.S. (2004). Iron partitioning between basaltic melts and clinopyroxene as a function of oxygen fugacity. *American Mineralogist*, 89, 1685-1693.

McLean, N.M., Bowring, J.F., & Bowring, S.A. (2011). An algorithm for U-Pb isotope dilution data reduction and uncertainty propagation. *Geochemistry, Geophysics, Geosystems*, 12, Q0AA18.

Moussallam, Y., Edmonds, M., Scaillet, B., Peters, N., Gennaro, E., Sides, I., & Oppenheimer, C. (2016). The impact of degassing on the oxidation state of basaltic magmas: A case study of Kilauea volcano. *Earth and Planetary Science Letters*, 450, 317-325.

Murphy, M.D., Sparks, R.S.J., Barclay, J., Carroll, M.R., Lejeune, A.M., Brewer, T.S., MacDonald, R., Black, S., & Young, S. (1998). The role of magma mixing in triggering the current eruption at the Soufriere Hills Volcano, Montserrat, West Indies. Geophysical Research Letters, 25, 3433-3436.

O'Neill, H.St.C. (1987). Quartz-fayalite-iron and quartz-fayalite-magnetite equilibria and the free energy of formation of fayalite (Fe_2SiO_4) and magnetite (Fe_3O_4). *American Mineralogist*, 72, 67-75.

O'Neill, H.StC. (2015). The effect of sulfide dissolved in silicate melts on enhancing the solubility of the Highly Siderophile Elements. American Geophysical Union, Fall Meeting 2015, abstract V52A-04.

O'Neill, H.St.C. (2016). The smoothness and shapes of chondrite-normalized rare earth element patters in basalts. *Journal of Petrology*, 57, 1463-1508.

O'Neill, H.St.C., & Eggins, S.M. (2002). The effect of melt composition on trace element partitioning: An experimental investigation of the activity coefficients of FeO, NiO, CoO, MoO_2 and MoO_3 in silicate melts. *Chemical Geology*, 186, 151-181.

O'Neill, H.St.C., & Navrotsky, A. (1984). Cations distributions and thermodynamic properties of binary spinel solid solutions. *American Mineralogist*, 69, 733-753.

O'Neill, H.St.C., Berry, A.J., & Eggins, S.M. (2008). The solubility and oxidation state of tungsten in silicate melts: Implications for the comparative chemistry of W and Mo in planetary differentiation processes. *Chemical Geology*, 255, 346–359

O'Neill, H.St.C., Dingwell, D.B., Borisov, A., Spettel, B, & Palme, H. (1995). Experimental petrochemistry of some highly siderophile elements at high temperatures, and some implications for core formation and the mantle's early history. *Chemical Geology*, 120, 255-273.

O'Neill, H.St.C., McCammon, C., Canil, D., Rubie, D.C., Ross, C.R., & Seifert, F. (1993). Mössbauer spectroscopy of mantle transition zone phases and determination of minimum Fe^{3+} content. *American Mineralogist*, 78, 456-460.

Ohashi, H., Fujita, T. & Osawa, T. (1982). The crystal structure of $NaTiSi_2O_6$ pyroxene. *The Journal of the Japanese Association of Mineralogists, Petrologists and Economic Geologists*, 77, 305-309.

Ottonello, G., Moretti, R., Marini, L. & Zuccolini, M.V. (2001). Oxidation state of iron in silicate glasses and melts: a thermochemical model. *Chemical Geology*, 174, 157-179.

Palme, H., & O'Neill, H.St.C. (2014), Cosmochemical estimates of mantle composition. In: Treatise on Geochemistry, 2nd Edition, Chapter 3.1, 1-39.

Papike, J.J., Karner, J.M., & Schearer, C.K. (2005). Comparative planetary mineralogy: Valence state partitioning of Cr, Fe, Ti, and V among crystallographic sites of olivine, pyroxene, and spinel from planetary basalts. *American Mineralogist*, 90, 277-290.

Papike, J.J., Burger, P.V., Bell, A.S., Shearer, C.K., Le, L., & Jones, J. (2015). Normal to inverse transition in martian spinel: Understanding the interplay between chromium, vanadium, and iron valence state partitioning through a crystal-chemical lens. *American Mineralogist*, 100, 2018-2025.

Papike, J.J., Simon, S.B., Burger, P.V., Bell, A.S., Shearer, C.K., & Karner, J.M. (2016). Chromium, vanadium, and titanium valence systematics in Solar System pyroxene as a recorder of oxygen fugacity, planetary provenance, and processes. *American Mineralogist*, 101, 907-918.

Park, J.W., Kamenetsky, V., Campbell, I., Park, G., Hanski, E., & Pushkarev, E. (2017). Empirical constraints on partitioning of platinum group elements between Cr-spinel and primitive terrestrial magmas. *Geochimica et Cosmochimica Acta*, 216, 393-416.

Pedersen, A.K. (1981). Armalcolite-bearing Fe-Ti oxide assemblages in graphite-equilibrated sialic volcanic rocks with native iron from Disko, central West Greenland. *Contributions to Mineralogy and Petrology*, 77, 307-324.

1237 Peters, M.T., Shaffer, E.E., Burnett, D.S., & Kim, S.S. (1995). Magnesium and titanium partitioning
1238 between anorthite and Type B CAI liquid: Dependence on oxygen fugacity and liquid
1239 composition. *Geochimica et Cosmochimica Acta*, 59, 2785-2796.

1240 Phinney, W.C. (1992). Partition coefficients for iron between plagioclase and basalt as a function
1241 of oxygen fugacity: Implications for Archean and lunar anorthosites. *Geochimica et*
1242 *Cosmochimica Acta*, 56, 1885-1895.

1243 Popp, R.K., Virgo, D., Yoder, H.S., Hoering, T.C. & Phillips, M.W. (1995). An experimental study of
1244 phase equilibria and Fe oxy-component in kaersutitic amphibole: Implications for the fH_2
1245 and aH_2O in the upper mantle. *American Mineralogist*, 80, 534-548.

1246 Poustovetov, A.A., & Roeder, P.L. (2000). The distribution of Cr between basaltic melt and
1247 chromium spinel as an oxygen geobarometer. *Canadian Mineralogist*, 39, 309-317.

1248 Rhodes, J.M., & Vollinger, M.J. (2005). Ferric/ferrous ratios in 1984 Mauna Loa lavas: A
1249 contribution to understanding the oxidation state of Hawaiian magmas. *Contributions to*
1250 *Mineralogy and Petrology*, 149, 666-674.

1251 Righter, K. & Shearer C.K. (2003). Magmatic fractionation of Hf and W: Constraints on the timing
1252 of core formation and differentiation in the Moon and Mars. *Geochimica et Cosmochimica*
1253 *Acta*, 67, 2497-2507.

1254 Righter, K., Sutton, S.R., Newville, M., Le, L., Schwandt, C.S., Uchida, H., Lavina, B., & Downs, R.T.
1255 (2006a). An experimental study of the oxidation state of vanadium in spinel and basaltic
1256 melt with implications for the origin of planetary basalt. *American Mineralogist*, 91, 1643-
1257 1656.

1258 Righter, K., Leeman, W.P, & Hervig, R.L. (2006b). Partitioning of Ni, Co and V between spinel-
1259 structured oxides and silicate melts: Importance of spinel composition. *Chemical Geology*,
1260 227, 1-25.

1261 Righter, K., Sutton, S., Danielson, L., Pando, K., Schmidt, G., Yang, H., Berthet, S., Newville, M.,
1262 Choi, Y., Downs, R.T., & Malavergne, V. (2011). The effect of fO_2 on the partitioning and
1263 valence of V and Cr in garnet/melt pairs and the relation to terrestrial mantle V and Cr
1264 content. *American Mineralogist*, 96, 1278-1290.

1265 Righter, K., Danielson, L.R., Pando, K.M., Shofner, G.A., Sutton, S.R., Newville, M., & Lee, C.T.
1266 (2016). Valence and metal/silicate partitioning of Mo: implications for conditions of Earth
1267 accretion and core formation. *Earth and Planetary Science Letters*, 437, 89-100.

1268 Roeder, P.L. & Reynolds, I. (1991). Crystallization of chromite and chromium solubility in
1269 basaltic melts. *Journal of Petrology*, 32, 909-934.

1270 Sato, M. (1978). Oxygen fugacity of basaltic magmas and the role of gas-forming elements.
1271 *Geophysical Research Letters*, 5, 447-449.

1272 Schärer, U., Berndt, J. & Deutsch, A. (2011). The genesis of deep-mantle xenocrystic zircon and
1273 baddeleyite megacrysts (Mbuji-Mayi kimberlite): Trace-element patterns. *European Journal*
1274 *of Mineralogy*, 23, 241-255.

1275 Schreiber, H.D. (1977). Redox states of Ti, Zr, Hf, Cr, and EU in basaltic magmas-an experimental
1276 study. Lunar and Planetary Science Conference Proceedings 8, 1785-1807.

1277 Schreiber, H.D. (1983). The chemistry of uranium in glass-forming aluminosilicate melts.
1278 *Journal of the Less Common Metals*, 91, 129-147.

1279 Schreiber, H.D., & Haskin, L.A. (1976). Chromium in basalts: Experimental determination of
1280 redox states and partitioning among synthetic silicate phases. 7th Lunar and Planetary
1281 Science Conference, 1221-1259.

1282 Schreiber, H.D., Merkel, R.C., Schreiber, L.V., & Balazs, G.B. (1987). Mutual interactions of redox
1283 couples via electron exchange in silicate melts: Models for geochemical systems. *Journal of*
1284 *Geophysical Research*, 92, 9233-9245.

1285 Shannon, R.D. (1976). Revised effective ionic radii and systematic studies of inter-atomic
1286 distance in halides and chalcogenides. *Acta Cyrstallographica*, 32, 751–767.

1287 Shearer, C.K., McKay, G., Papike, J.J., & Karner, J.M. (2006). Valence state partitioning of
1288 vanadium between olivine-liquid: Estimates of the oxygen fugacity of Y980459 and
1289 application to other olivine-phyric martian basalts. *American Mineralogist*, 91, 1657-1663.

1290 Shim, S-H., Grocholski, B., Ye, Y., Alp, E.E., Xu, S., Morgan, D., Meng, Y., & Prakapenka, V.B. (2017).
1291 Stability of ferrous-iron-rich bridgmanite under reducing midmantle conditions. *PNAS*, 114,
1292 6468-6473.

1293 Sievwright, R.H., Wilkinson, J.J., O'Neill, H.St.C., & Berry, A.J. (2017). Thermodynamic controls on
1294 element partitioning between titanomagnetite and andesitic-dacitic melts. *Contributions to*
1295 *Mineralogy and Petrology*, 172, 62.

1296 Simon, S.B., & Sutton, S. R. (2018). Valences of Ti, Cr, and V in Apollo 17 high-Ti and very low-Ti
1297 basalts and implications for their formation. *Meteoritics & Planetary Science*, 53, 2138-2154.

1298 Smythe, D.J., & Brenan, J.M. (2015). Cerium oxidation state in silicate melts: Combined fO_2,
1299 temperature and compositional effects. *Geochimica et Cosmochimica Acta*, 170, 173-187.

1300 Smythe, D.J., & Brenan, J.M. (2016). Magmatic oxygen fugacity estimated using zircon-melt
1301 partitioning of cerium. *Earth and Planetary Science Letters*, 453, 260-266.

1302 Sommer, J. (2014). Experimental study: Solubility of Pt and Rh in silicate melt as a function of
1303 silicate melt compositions, temperature and oxygen fugacity. MSc Thesis, University of Bonn,
1304 Germany.

1305 Sun, C.-O., Williams, R.J., & Sun, S.-S. (1974). Distribution coefficients of Eu and Sr for
1306 plagioclase-liquid and clinopyroxene-liquid equilibria in oceanic ridge basalt: An
1307 experimental study. *Geochimica et Cosmochimica Acta*, 38, 1415–1433.

1308 Sutton, S.R., & Newville, M. (2014). Synchrotron x-ray spectroscopic analysis. In: Treatise on
1309 Geochemistry, 2nd Edition, H. Holland and K. Turekian (eds.), v. 15, p. 213-230.

1310 Sutton, S.R., Goodrich, C.A., & Wirick, S. (2017). Titanium, vanadium and chromium valences in
1311 silicates of ungrouped achondrite NWA 7325 and ureilite Y-791538 record highly-reduced
1312 origins. *Geochimica et Cosmochimica Acta*, 204, 313-330.

1313 Sutton, S.R., Karner, J., Papike, J., Delaney, J.S., Shearer, C., Newville, M., Eng, P., Rivers, M., & Dyar,
1314 M.D. (2005). Vanadium K edge XANES of synthetic and lunar basaltic glasses and application
1315 to microscale oxygen barometry. *Geochimica et Cosmochimica Acta*, 69, 2333-2348.

1316 Thomson, A.R., Kohn, S.C., Bulanova, G.P., Smith, C.B., Araujo, D., & Walter, M.J. (2016). Trace
1317 element composition of silicate inclusions in sub-lithospheric diamonds from the Juina-5
1318 kimberlite: Evidence for diamond growth from slab melts. *Lithos*, 265, 108-124.

1319 Toplis, M.J., & Corgne, A. (2002). An experimental study of element partitioning between
1320 magnetite, clinopyroxene and iron-bearing silicate liquids with particular emphasis on
1321 vanadium. *Contributions to Mineralogy and Petrology*, 144, 22-37.

1322 Trail, D., Watson, E.B., & Tailby, N.D. (2011). The oxidation state of Hadean magmas and
1323 implications for early earth's atmosphere. *Nature*, 480, 79-82.

1324 Trail, D., Watson, E.B., & Tailby, N.D. (2012). Ce and Eu anomalies in zircon as proxies for the
1325 oxidation state of magmas. *Geochimica et Cosmochimica Acta*, 97, 70-87.

van Kan Parker, M., Mason, P.R.D. & van Westrenen, W. (2011). Experimental study of trace element partitioning between lunar orthopyroxene and anhydrous silicate melt: Effects of lithium and iron. *Chemical Geology*, 285, 1-14.

Wade, J., Wood, B.J., & Norris, A. (2013). The oxidation state of tungsten in silicate melt at high pressures and temperatures. *Chemical Geology*, 335, 189–193.

Wade, J., Wood, B.J., & Tuff, J. (2012). Metal–silicate partitioning of Mo and W at high pressures and temperatures: evidence for late accretion of sulphur to the Earth. *Geochimica et Cosmochimica Acta*, 85, 58-74.

Wadhwa, M. (2008). Redox conditions on small bodies, the Moon and Mars. *Reviews in Mineralogy and Geochemistry*, 68, 493-510.

Wijbrans, C.H., Klemme, S., Berndt, J., & Vollmer, C. (2015). Experimental determination of trace element partition coefficients between spinel and silicate melt: The influence of chemical compositions and oxygen fugacity. *Contributions to Mineralogy and Petrology*, 169, 45.

Wilke, M., & Behrens, H. (1999). The dependence of the partitioning of iron and europium between plagioclase and hydrous tonalitic melt on oxygen fugacity. *Contributions to Mineralogy and Petrology*, 137, 102-114.

Wood, B.J., & Blundy, J.D. (2003). Trace element partitioning under crustal and upper mantle conditions: The influences of ionic radius, cation charge, pressure, and temperature. In: Treatise on Geochemistry, vol. 2, chapter 2.09, R.W Carlson (Ed.), p. 395-424.

Woodhead, J.D. (1989). Geochemistry of the Mariana arc (western Pacific): Source composition and processes. *Chemical Geology*, 76, 1-24.

Young, E.D., Dyl, K.A., & Simon, J.I. (2012). Response to the Comment by SB Simon, L. Grossman, and SR Sutton on "Valence state of titanium in the Wark-Lovering rim of a Leoville CAI as a record of progressive oxidation in the early Solar Nebula". *Geochimica et Cosmochimica Acta*, 85, 377-382.

Figure captions

Figure 1. (a) Schematic illustration of lattice strain parameters D_0, r_0 and E for the mineral/melt partition coefficient (D) of an element i as modelled by the Brice equation (Blundy and Wood, 1994); $D_\mathrm{i} = D_0 \exp([-4\pi E N_A(r_0 - r_\mathrm{i})^2 - 1/3(r_0 - r_\mathrm{i})^3]/RT)$, and **(b, c, d)** measured changes in these parameters with cation valence state (i.e. charge) as determined experimentally for $CaSiO_3$/melt partitioning (Law et al., 2000).

Figure 2. Relative oxygen fugacity conditions (in log units relative to FMQ, the fayalite-magnetite-quartz buffer; values from O'Neill, 1987) for several planetary geochemical reservoirs (Frost and McCammon, 2008; Grossman et al. 2008; Wadhwa, 2008), and valence state transition ranges for the elements discussed in this chapter. See text for references. Also plotted for reference the IW (Fe-FeO), NNO (Ni-NiO), and HM (hematite-magnetite) buffers.

Figure 3: Mineral/melt partitioning of transition metals as a function of oxygen fugacity (in log units relative to FMQ, the fayalite-magnetite-quartz buffer; values from O'Neill, 1987) for selected minerals. Abbreviations: amph - amphibole, cpx - clinopyroxene, opx - orthopyroxene, olv - olivine, plag - plagioclase feldspar, spl - spinel, zrc - zircon. All curves shown in the main diagram are best fits of the experimental data to an equation with the same form as Equation 22. The fraction (from 0 to 1) of the different valence states of each element are plotted on top of the diagram. These were calculated using Equation 13 using available data. **(a)** Fe mineral/melt partitioning data from King et al., 2000 (amph), Mallmann and O'Neill, 2009 (spl,

olv, opx, cpx) and Phinney, 1992 (plag). **(b)** Cr mineral/melt partitioning data from Mallmann and O'Neill, 2009 (olv, opx, cpx). **(c)** Ti mineral/melt partitioning data from Mallmann and O'Neill, 2009 (olv, opx, cpx), Peters et al. 1995 (plag) and Burnham and Berry, 2012 (zrc). **(d)** (d) V mineral/melt partitioning data from Mallmann and O'Neill, 2009 (olv, opx, cpx, spl).

Figure 4. Comparison of Cr olivine(Fo_{100})/melt partitioning coefficients obtained at 1 bar and 1320 °C as a function of oxygen fugacity (in log units relative to FMQ, the fayalite-magnetite-quartz buffer; values from O'Neill, 1987) for three Fe-free compositions in the CaO-MgO-Al_2O_3-SiO_2 system: FAS1, FAD1 and FAD3 (Hanson and Jones, 1998). The results illustrate a mild effect of melt composition on the partitioning of Cr^{3+} yet no significant effect on the partitioning of Cr^{2+}. The fraction (from 0 to 1) of the different valence states are plotted on top of the diagram.

Figure 5. Zircon/melt partition coefficients for REE elements determined experimentally at 1 bar as a function of oxygen fugacity by Burnham and Berry (2012). The colored segments highlight systematic changes in the partitioning of Ce and Eu with oxygen fugacity (labelled relative to the FMQ buffer).

Figure 6. Mineral/melt partitioning of redox-sensitive rare earth elements (REE), Ce **(a)** and Eu **(b)** as a function of oxygen fugacity (in log units relative to FMQ, the fayalite-magnetite-quartz buffer; values from O'Neill, 1987) for selected minerals. Abbreviations: bdd - baddeleyite, cpx - clinopyroxene (aluminous diopside), olv - olivine, opx - orthopyroxene, plag - plagioclase feldspar, ttn - titanite, zrc - zircon. Where data were not obtained as a function of fO_2, partition coefficients for Ce^{3+}, Ce^{4+}, Eu^{2+} and Eu^{3+} (or estimates thereof) were used in conjunction with the $Ce^{4+}/\Sigma Ce$ and $Eu^{3+}/\Sigma Eu$ models of Burnham and Berry (2014) and Burnham et al. (2015). Data from Klemme and Meyer, 2003 (bdd), Leitzke et al., 2017 (cpx-Ce, plag-Ce, olv), Sun et al., 1974 (cpx-Eu, plag-Eu, opx-Eu), van Kan Parker et al., 2011 (opx-Ce), Bachmann et al., 2005 (ttn), and Burnham and Berry, 2012 (zrc). See Fig. 3 for more details.

Figure 7. Mineral/melt partitioning of U as a function of oxygen fugacity (in log units relative to FMQ, the fayalite-magnetite-quartz buffer; values from O'Neill, 1987) for selected minerals. Abbreviations: cpx - clinopyroxene (diopside), olv - olivine, opx - orthopyroxene, zrc - zircon. Data from Fonseca et al., 2014 (opx, cpx, olv), and Burnham and Berry, 2012 (zrc). See Fig. 3 for more details.

Figure 8. Mineral/melt partitioning of siderophile elements (Mo, W and Re) as a function of oxygen fugacity (in log units relative to FMQ, the fayalite-magnetite-quartz buffer; values from O'Neill, 1987) for selected minerals. Abbreviations: cpx - clinopyroxene, opx - orthopyroxene, olv - olivine, spl - spinel, grt - garnet. Data from Leitzke et al., 2017 (Mo: cpx, opx, olv), Wijbrans et al., 2015 (Mo: spl), Fonseca et al., 2014 (W: opx, cpx, olv), and Mallmann and O'Neill, 2007 (Re: cpx, opx, spl, grt, ol). See Fig. 3 for more details.

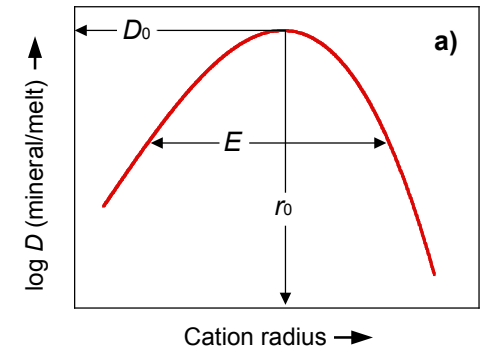
a)
D_0
E
r_0
log D (mineral/melt)
Cation radius

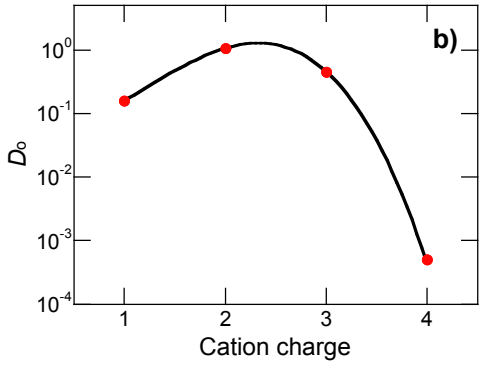
b)
10^0
10^{-1}
10^{-2}
10^{-3}
10^{-4}
D_o
1
2
3
4
Cation charge

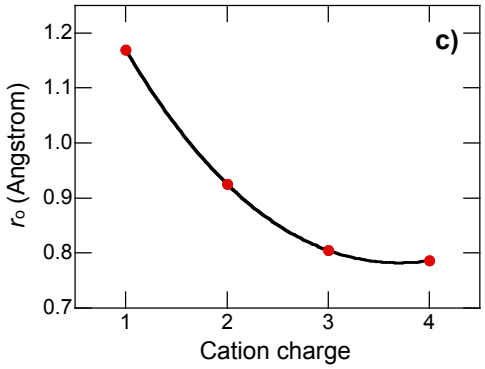
c)
1.2
1.1
1.0
0.9
0.8
0.7
r_o (Angstrom)
1
2
3
4
Cation charge

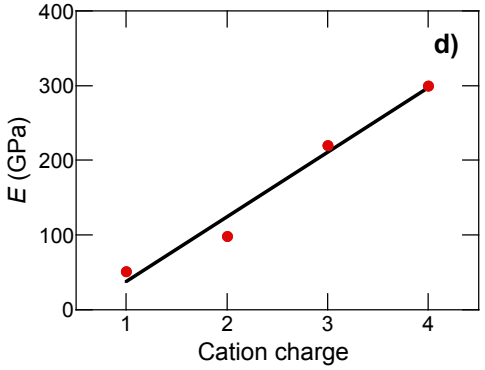
d)
400
300
200
100
0
E (GPa)
1
2
3
4
Cation charge

Figure 2

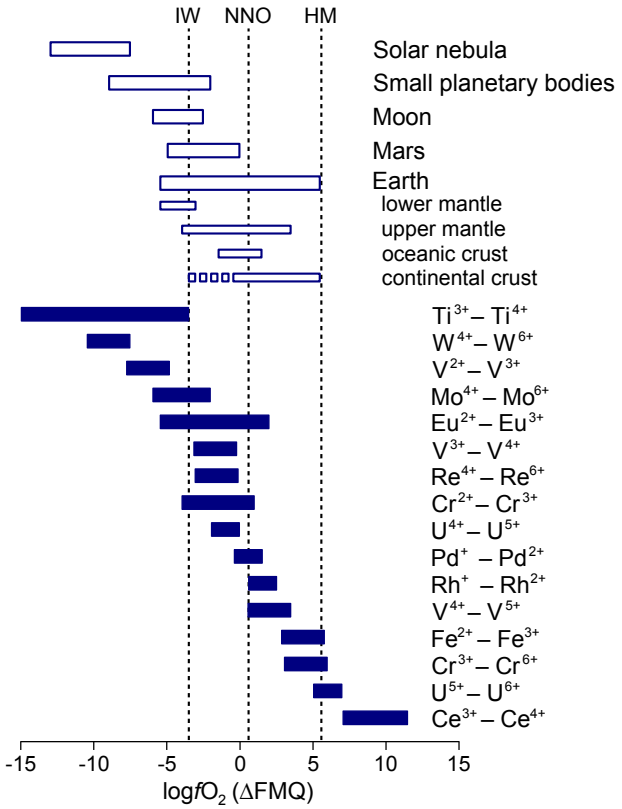
IW
NNO
HM
Solar nebula
Small planetary bodies
Moon
Mars
Earth
lower mantle
upper mantle
oceanic crust
continental crust
Ti3+ – Ti4+
W4+ – W6+
V2+ – V3+
Mo4+ – Mo6+
Eu2+ – Eu3+
V3+ – V4+
Re4+ – Re6+
Cr2+ – Cr3+
U4+ – U5+
Pd+ – Pd2+
Rh+ – Rh2+
V4+ – V5+
Fe2+ – Fe3+
Cr3+ – Cr6+
U5+ – U6+
Ce3+ – Ce4+
-15
-10
-5
0
5
10
15
logfO2 (ΔFMQ)

Figure 3

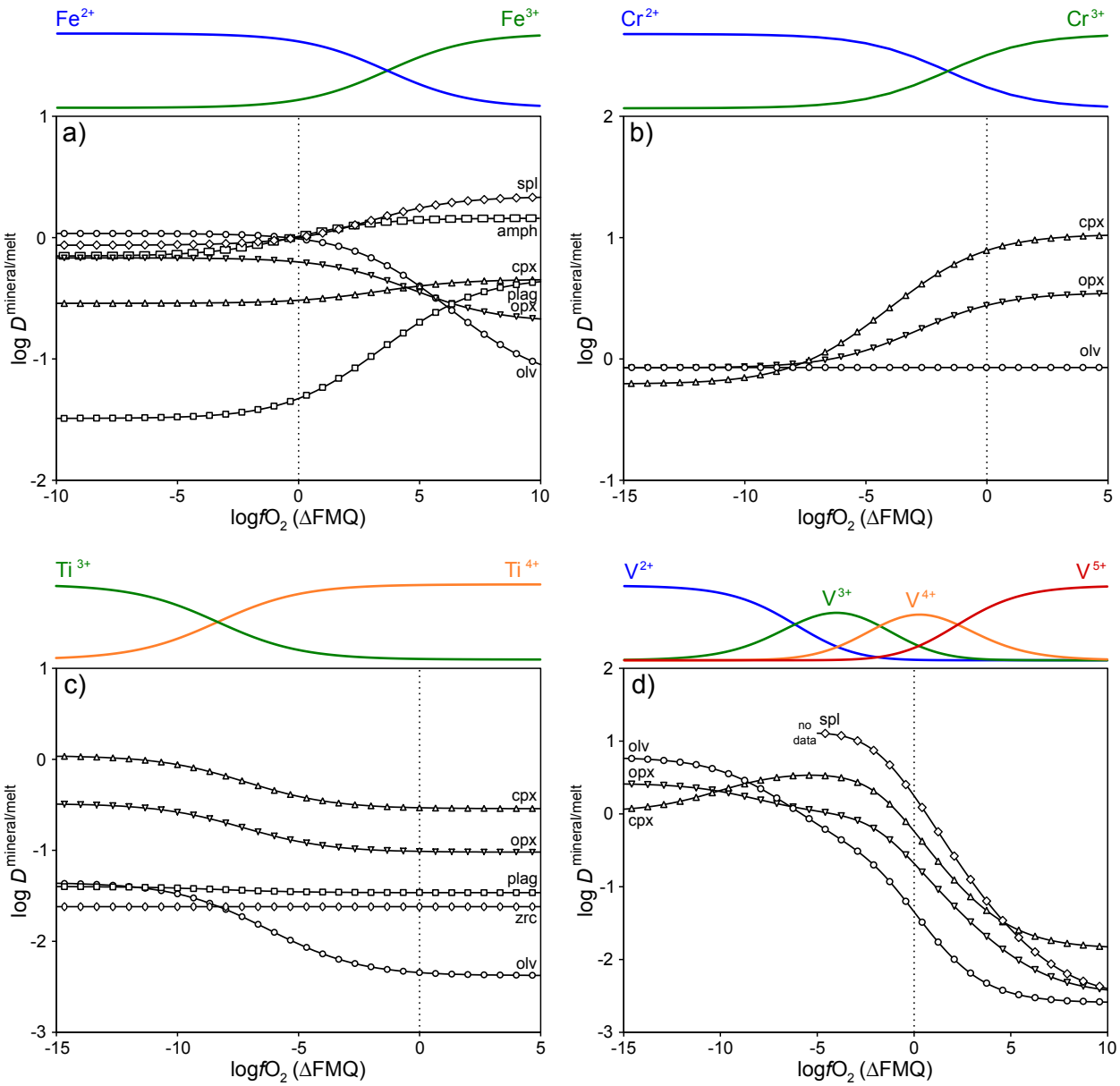
Fe2+
Fe3+
a)
spl
amph
cpx
plag
opx
olv
log D mineral/melt
logfO2 (ΔFMQ)
Cr2+
Cr3+
b)
cpx
opx
olv
log D mineral/melt
logfO2 (ΔFMQ)
Ti 3+
Ti 4+
c)
cpx
opx
plag
zrc
olv
log D mineral/melt
logfO2 (ΔFMQ)
V2+
V3+
V4+
V5+
d)
no data
spl
olv
opx
cpx
log D mineral/melt
logfO2 (ΔFMQ)

Figure 4

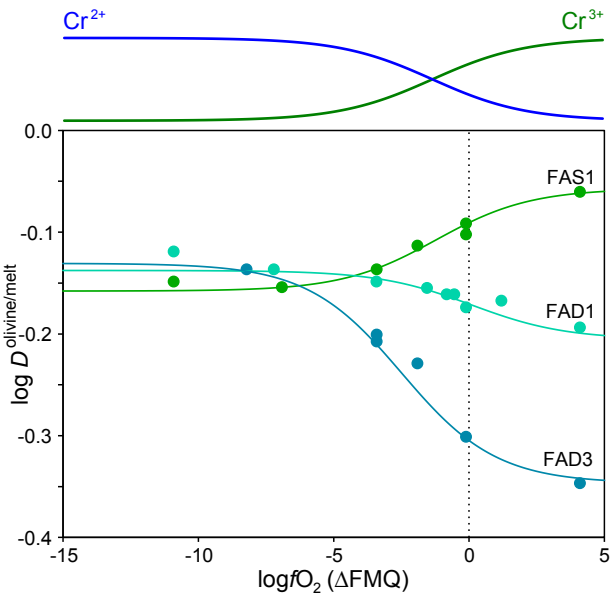
Cr2+
Cr3+
0.0
-0.1
-0.2
-0.3
-0.4
log D olivine/melt
FAS1
FAD1
FAD3
-15
-10
-5
0
5
logfO2 (ΔFMQ)

Figure 5

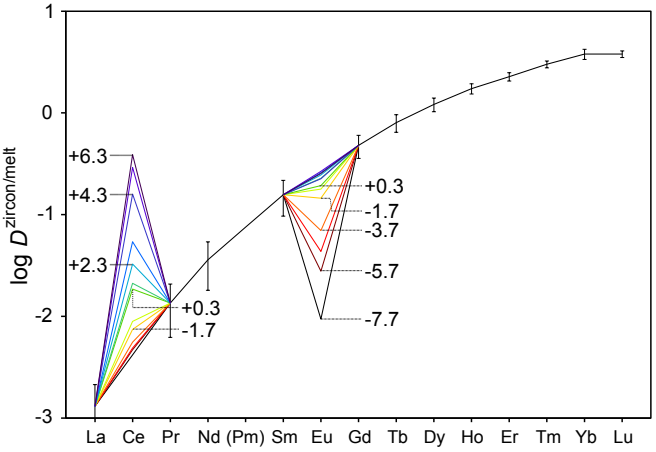
1
0
-1
-2
-3
log D zircon/melt
+6.3
+4.3
+2.3
+0.3
-1.7
+0.3
-1.7
-3.7
-5.7
-7.7
La
Ce
Pr
Nd
(Pm)
Sm
Eu
Gd
Tb
Dy
Ho
Er
Tm
Yb
Lu

Figure 6

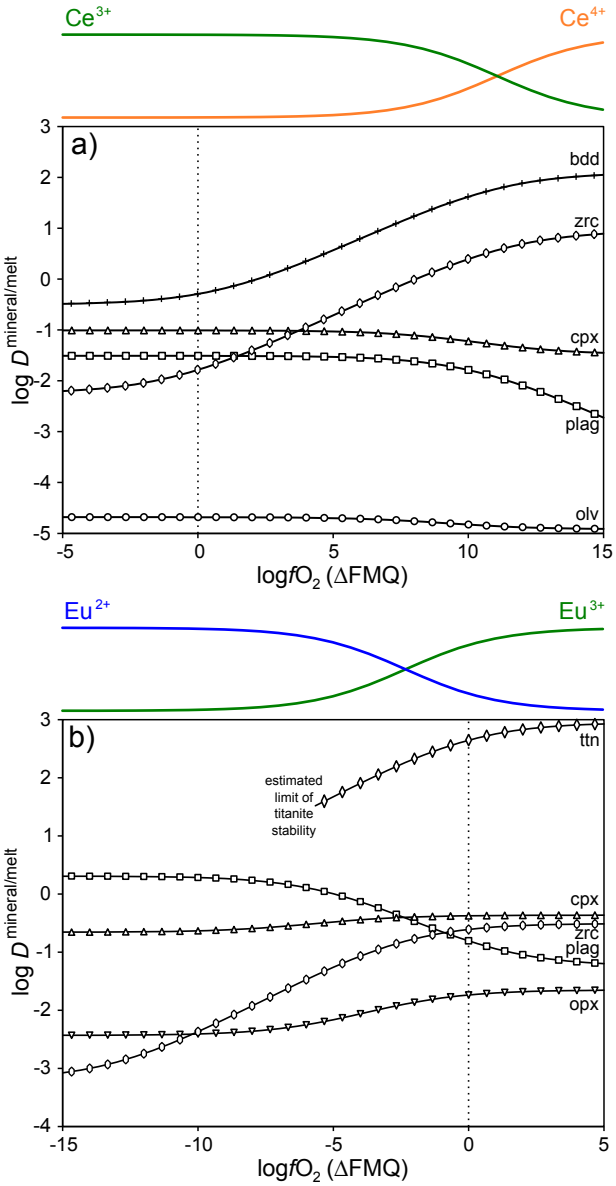
Ce3+
Ce4+
a)
bdd
zrc
cpx
plag
olv
log D mineral/melt
logfO2 (ΔFMQ)
Eu2+
Eu3+
b)
ttn
estimated limit of titanite stability
cpx
zrc
plag
opx
log D mineral/melt
logfO2 (ΔFMQ)

Figure 7

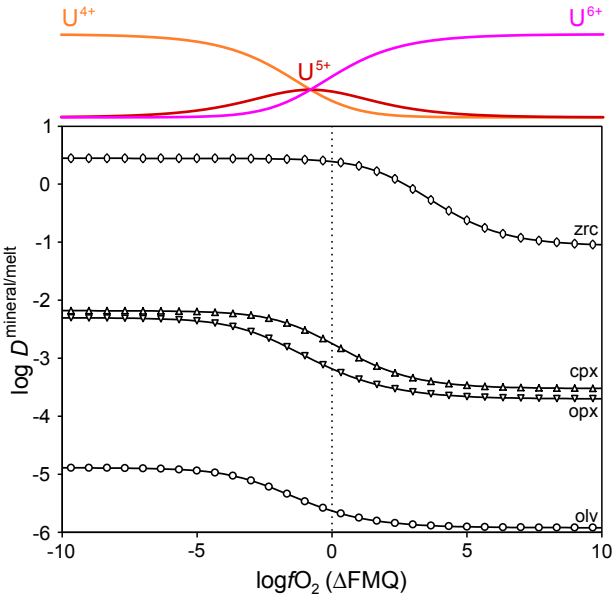
U4+
U6+
U5+
1
0
-1
-2
-3
-4
-5
-6
log D mineral/melt
zrc
cpx
opx
oly
-10
-5
0
5
10
logfO2 (ΔFMQ)

Figure 8

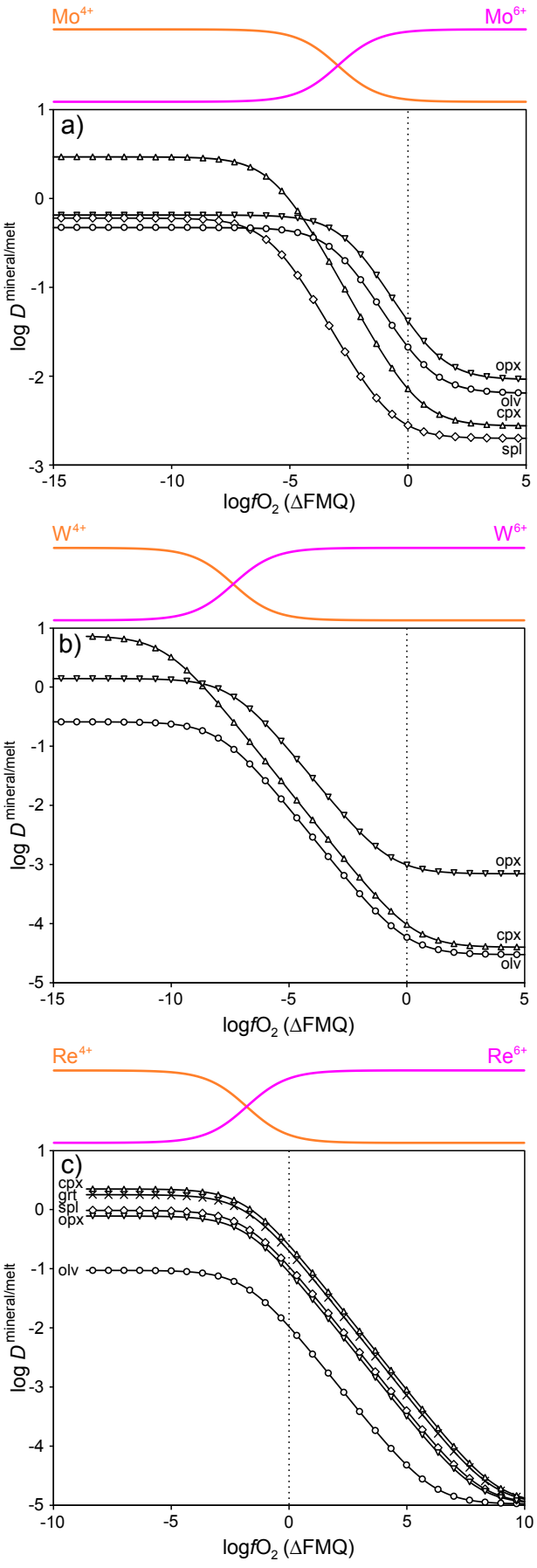
Mo4+
Mo6+
a)
log D mineral/melt
opx
olv
cpx
spl
logfO2 (ΔFMQ)
W4+
W6+
b)
log D mineral/melt
opx
cpx
olv
logfO2 (ΔFMQ)
Re4+
Re6+
c)
cpx
grt
spl
opx
olv
log D mineral/melt
logfO2 (ΔFMQ)